Kinematics of fault-related folding derived from a sandbox experiment

Sylvain Bernard[1,*], Jean Philippe Avouac[1], Stéphane Dominguez[2], Martine Simoes[1,**]

[1] *Tectonics Observatory, California Institute of Technology, Pasadena, USA.*

[2] *Laboratoire Dynamique de la Lithosphère, ISTEEM, Montpellier, France.*

[*] now at Laboratoire de Géologie, Ecole Normale Supérieure, Paris, France.

[**] now at Géosciences Rennes, Université Rennes 1, France

Abstract

We analyze the kinematics of fault-tip folding at the front of a fold-and-thrust wedge using a sandbox experiment. The analog model consists of sand layers intercalated with low friction glass bead layers, with a total thickness h = 4.8 cm, deposited in a glass sided experimental device. A computerized mobile backstop induces progressive horizontal shortening of the sand layers and consequently thrust fault propagation. Active deformation at the tip of the forward propagating basal décollement is monitored along the cross section with a high resolution CCD camera, and the displacement field between pairs of images is measured from the optical flow technique. In the early stage, when cumulative shortening is less than about h/10, slip along the décollement tapers gradually to zero and the displacement gradient is absorbed by

distributed deformation of the overlying medium. In this stage of detachment-tip folding, horizontal displacements decrease linearly with distance towards the foreland. Vertical displacements reflect a nearly symmetrical mode of folding, with displacements varying linearly between relatively well-defined axial surfaces. When the cumulative slip on the décollement exceeds about $h/10$, deformation tends to localize on a few discrete shear bands at the front of the system, until shortening exceeds $h/8$ and deformation gets fully localized on a single emergent frontal ramp. The fault geometry subsequently evolves to a sigmoid shape and the hanging wall deforms by simple shear as it overthrusts the flat-ramp system. As long as strain localization is not fully established the sand layers experience a combination of thickening and horizontal shortening which induce gradual limb rotation. The observed kinematics can be reduced to simple analytical expressions that can be used to restore fault-tip folds, relate finite deformation to incremental folding, and derive shortening rates from deformed geomorphic markers or growth strata.

1. Introduction

Abandoned fluvial or alluvial terraces, as well as growth strata can be used to determine incremental deformation associated with active folds [*e.g.*, *Rockwell, et al.*, 1988; *Suppe, et al.*, 1992; *Hardy and Poblet*, 1994; *Molnar, et al.*, 1994; *Hardy, et al.*, 1996; *Storti and Poblet*, 1997; *Lavé and Avouac*, 2000; *van der Woerd, et al.*, 2001; *Thompson, et al.*, 2002]. If a unit can be traced all the way across a given fold it can be used to estimate uplift since its deposition, and then to derive the corresponding average shortening from a mass balance calculation [*Chamberlin*, 1910; *Epard and Groshong*, 1993] (Figure 1). Although this geometrical approach can be used to estimate cumulative shortening, it can only rarely be applied to geomorphic markers since a terrace record is often discontinuous and buried below younger sediments in the foreland or in piggyback basins. An alternative approach consists in fitting the terrace record from a model of folding constrained from pre-growth strata (structural measurements or subsurface data). This approach has been applied to fault-bend folds (Figure 2A) assuming that the hanging wall deforms by flexural-slip folding [*Lavé and Avouac*, 2000; *Thompson, et al.*, 2002]. In such a case, where both bed length and thickness are constant, the local uplift U relative to the footwall, assumed rigid, obeys

$$U(x) = i(x) + b = R(z) \cdot \sin\theta(x) \quad (1)$$

where x is the distance along the section line; $i(x)$ is the river incision since terrace abandonment; b is the base level change since terrace abandonment (positive upward); $\theta(x)$ is the local bedding dip angle; and $R(z)$ is the horizontal shortening since terrace abandonment of the layer at elevation z, which crops out at distance x from the trailing edge of the section (Figure 1). Base level change may lead to either entrenchment ($b<0$) or aggradation ($b>0$) in the foreland. On the

sketch in Figure 1, we have assumed no bed-parallel shear away from the fault zone, hence R is independent of z. In that case, estimating R does not require a continuous terrace profile and it is sufficient to use only a few independent estimates of the entrenchment rate at places with different dip angles in the zone where the bedding is already parallel to the fault plane (i.e. backlimb of the fold represented in Figure 1). In principle, estimates of incision rate at at least two points with different dip angles are necessary to derive both R and b [*Thompson, et al.*, 2002]. When sufficiently complete terrace records are available, the relationship expressed by (1) is testable since it predicts that uplift and the sinus of the local bedding dip angle, $\sin(\theta)$, are proportional. Irrespective of the geomorphic record, it is important to note that this approach does not apply all along the profile of the fold, but only where the bedding is parallel to the fault plane (Figures 1 and 2B).

Fault-tip folds can develop by distributed pure shear, with requisite bed length and thickness changes associated with limb rotation [*Dahlstrom*, 1990; *Erslev*, 1991; *Poblet and McClay*, 1996; *Mitra*, 2003], or by kink-band migration and bed-parallel simple shear, as in the case of fault-propagation folds [*Suppe and Medwedeff*, 1990; *Mosar and Suppe*, 1992]. In either case, beds near the surface are not everywhere parallel to the thrust fault at depth, so that equation (1) does not hold in places like the fold forelimb in Figure 1. Figure 2B shows a number of acceptable kinematic models of fault-tip folds, all based on the assumption of mass conservation. Most of these models are commonly used to guide interpretation of structural measurements or seismic profiles [*Erslev*, 1991; *Mosar and Suppe*, 1992; *Wickham*, 1995; *Storti and Poblet*, 1997; *Allmendinger*, 1998; *Allmendinger and Shaw*, 2000; *Brooks, et al.*, 2000; *Zehnder and Allmendinger*, 2000; *Mitra*, 2003]. In contrast to these purely geometric models, some authors have explored the possibility of modeling folds from the theory of elastic

dislocations in an elastic half-space [*Myers and Hamilton*, 1964; *King, et al.*, 1988; *Stein, et al.*, 1988; *Ward and Valensise*, 1994; *Savage and Cooke*, 2004]. Although any of these various fold models might be used to analyze growth strata or deformed alluvial terraces and retrieve the kinematic history of folding, two difficulties generally arise. One is that the choice of a kinematic model is not straightforward, even when growth strata geometry is well constrained. The other is that the mathematical implementation of these models and the adjustment to field data is generally not simple. For these reasons, we seek a simple alternative relationship linking local uplift and/or bedding tilt to structural geometry. This relationship must be applicable across an entire structure and must be grounded in realistic fold kinematics or mechanics. For this purpose, we analyze folding produced in an analogue experiment to derive some kinematic model.

It has been observed that the formation of the most frontal ramp in analogue models of wedge mechanics [*Dominguez, et al.,* 2001] is preceded by a phase of distributed deformation which resembles fault-tip folding. We therefore focused the present study on this particular phase, assuming it can be considered to simulate the kinematics of the early stage of fault-related folding at the natural scale. With this aim, we used a new experimental set-up that allows accurate measurements of fault slip kinematics and of the associated deformation field [*Dominguez, et al.*, 2003].

We first present the experimental set-up and the principles of the approach. We then describe in detail the evolution of incremental deformation during a representative experiment selected among more than 10 performed experiments, and derive some simple analytical approximations. Finally, we propose and test a procedure that can be used to restore incremental

or cumulative deformation across fault-tip folds. All variables introduced in the analysis are listed and defined in Table 1.

2. Experimental Set-up

The physical properties of dry sand and glass beads ($\phi_s \sim 30°$, low cohesion, time independent mechanical behaviour) make them good analogue materials to simulate brittle deformation of the upper crust at the laboratory scale [e.g. *Malavieille,* 1984; *Mulugeta,* 1988; *Mulugeta and Koyi*, 1992; *Koyi*, 1995; *Gutscher, et al.,* 1998; *Dominguez, et al*., 2000; *Adam et al,* 2005; *Konstantinovskaia and Malavieille*, 2005]. Experiments where the layers are overlying a rigid basement and are subjected to horizontal shortening produce a self-similar accretionary prism analogous to accretionary prisms formed along subduction zones or in intracontinental fold-and-thrust belts [*Chapple*, 1978; *Davis, et al.*, 1983; *Lallemand, et al.,* 1994; *Gutscher, et al.*, 1998]. These experiments lead to the formation of imbricated thrust sheets that gradually accrete to the wedge as the detachment propagates forward. In the absence of cohesion this process and the resulting geometries are scale independent. However, given the estimate of the cohesion of the material used in this experiment (C_o<50 Pa) and the typical cohesion of crustal rocks (C_o>20MPa [*Lallemand, et al.,* 1994; *Schellart*, 2000], the scaling factor can be estimated to about 10^5. Accordingly, 1 cm in the model is equivalent to about 1 km in nature.

The model box is 20 cm wide and 100 cm long and equiped with transparent side walls treated to reduce friction [*Dominguez et al.,* 2001]. The model comprises 6 sand layers, each 6-7 mm thick, intercalated with 5 glass bead layers, each 2 mm thick. The total model thickness, h, is 4.8 cm. We use this layering to simulate natural lithologic intercalations and stratigraphic

discontinuities, and to facilitate layer parallel shear, a process which is thought to be key to folding of sedimentary layers at the natural scale.

The sand and glass bead layers are deformed in front of a moving backstop activated by a step motor at a constant velocity of 235 ± 10 μm per minute (1.4 cm/h (Figure 3). The cohesion and friction angle of the materials was provided by the manufacturers (SIFRACO and EYRAUD) and also measured in our laboratory [*Krantz,* 1991; *Jolivet,* 2000; *Schellart,* 2000]. The sand has a fluvial origin with irregularly rounded grain shapes and sizes from 150 to 300 μm. Its internal friction angle is 30˚ to 35˚ ($\tan(\phi_s)$=0.6 to 0.7) and its cohesion is low (Co < 50 Pa). The glass beads are SiO2-Na2O, cohesionless microspheres with grain sizes ranging from 50 to 150 μm and an internal friction angle between 20˚ and 25˚ ($\tan\phi_g$=0.35 to 0.45). The model is built on a 2 cm thick, horizontal (β=0) polyvinyl chloride (PVC) plate. The basal friction along the sand/unpolished PVC interface is 21˚±4° ($\tan(\phi_b$= 0.38) [*Jolivet,* 2000].

Our experimental set-up was designed so as to measure, with the maximum possible accuracy, the deformation at the tip of the basal detachment and the formation of a new thrust fault at the front of the wedge. In order to avoid episodic re-activation of older internal faults and force the deformation to be localized at the very front of the wedge, we started the experiment with a 10° pre-deformation sandwedge. In experiments run with the same layering as the one described here we observed the formation of a wedge with a slope of 8-9° which is approximately the critical slope of about 8° of a homogeneous wedge predicted from the critical wedge theory given the value of the basal friction angle, ϕ_b, of 21° and the value of the internal friction angle, ϕ_s, of 30° for the sand mass [*Davis, et al.*, 1983]. This shows that the layering does not modify significantly the mechanical behavior of the accretionary wedge and that coulomb wedge theory can still be applied.

We focus on the foreland edge of the wedge, which grows by the forward propagation of the basal décollement. This part of the experiment is located about 15 cm from the backstop and, to ensure maximum spatial resolution, is the only portion of the experiment monitored with the video system (box in Figure 3). By comparing the imposed displacement of the backstop with displacements measured within the zone monitored by the video system, we find that during the selected experiment about 98% of the shortening is absorbed by internal deformation within the monitored frame. Photographs are taken with a constant sampling rate of 1 image/minute with a 6.3 megapixels CCD camera. The pixel size is 80 by 80 μm². Given that the backstop velocity and the sampling rate are constant, the incremental shortening between two successive images is constant and equals 235 +/- 10 μm. The displacement field between two successive images is measured from the optical flow technique, which was introduced by Horn and Schunk [1980] and commonly used in remote sensing and image processing for robotic applications. It applies to images with a brightness pattern that evolves only due to deformation of the medium, as is the case of our experiment. The technique allows a subpixel accuracy and appears more powerful than more recent correlation techniques such as Particle Imaging Velocimetry [*Adam, et al.,* 2005]. It is based on the fact that the image F at time $t+dt$, can be written:

$$F(t+dt) \approx F(t) + \nabla F(t) \cdot dX \qquad (2)$$

where dX is the displacement field and $\nabla F(t)$ is the spatial gradient of image $F(t)$. Equation (2) is only an approximation because higher order terms in the Taylor-Lagrange development are neglected. The gradient is estimated from Rider's method [*Press, et al.,* 1995]. The technique was first applied to the analysis of sandbox experiments by Dominguez, et al. [2001].

The displacement field varies smoothly and the signal to noise ratio is better when it is measured over few images (typically over 2-3 images). The correlation window is 32*32 pixels,

and is moved by increments of 8 pixels across the whole image. The displacement field thus contains 350*149 independent measurements, with a sampling (or spatial) resolution of 640 μm. Based on calibration tests, errors on measurements are statistically estimated to be less than 5 %. The horizontal and vertical components of the displacements are plotted separately and used to generate various representations such as displacement vectors or incremental deformation of a virtual grid (Figures 3 and 4). Because the measurements are made from pairs of images separated by variable time lags, incremental displacements are normalized by dividing them by the number of time steps (1 step corresponding to two successive images). Displacements are thus expressed in millimeters per step (mm/step), a step corresponding to a shortening of 235 +/- 10 μm, and are thus equivalent to normalized velocities. For our analysis we examine profiles across the horizontal and vertical displacement fields at different depths above the décollement.

Surface processes are not simulated in the model. Therefore, the analogue experiment does not directly reproduce growth strata nor deformed terraces. However, the mathematical description of folding derived from this experiment, as detailed below, can easily be used to simulated the expected geometry of growth strata or terraces [*Simoes, et al.*, this issue; *Daeron, et al.*, this issue].

3. From detachment-tip folding to ramp overthrusting

Deformation within the domain covered by the imaging system starts to become significant only after about image 10, which corresponds to 2.3 mm of shortening, or 5% of the initial thickness of the sand layers (h/20). Prior to this, deformation is entirely accommodated closer to the backstop, outside the area covered by the camera. Following this initial phase of shortening, the evolution of deformation can be divided into two main stages that are the focus of our analysis. The first stage comprises distributed deformation and tip-line folding above the

foreland edge of the horizontal basal detachment. The second deformation stage occurs after a brief transitional phase of strain localization, and consists of upward propagation of the detachment tip and of formation of a mature frontal thrust ramp. Hanging-wall material is subsequently transported along this new fault surface.

During the first stage of deformation, horizontal velocities decrease linearly with distance away from the backstop, and vertical velocities show a nearly symmetrical, trapezoidal pattern of uplift (Figure 5A). We separate the uplift pattern into domains in which incremental uplift varies linearly with horizontal distance, and interpret the boundaries of these domains as fold axial surfaces. The position of each of these surfaces was determined by the maximum change in slope of the uplift rate versus distance curve as calculated in several different horizons (Figure 6). The analysis of the evolving velocity fields during this stage of deformation allowed us to study the four identified axial surfaces kinematic behaviour.

The two outer axial surfaces (labelled 1 and 4 in Figure 7) initiate and remain in their same positions throughout the first stage of deformation. Axial surface 4 marks the frontal limit of the deforming zone and appears to be fixed to both the footwall and hanging wall, essentially acting as a foreland pin line. The discontinuity in the horizontal velocity field places this pin line 30 mm further to the foreland than the discontinuity in the vertical displacement field, suggesting there is a measurable, but small volume loss in the foreland adjacent to the growing fold. We believe this volume loss is a specific feature of the analogue model, and most likely results from a reorganization of sand grain packing that would not occur in a natural setting. The most hinterland axial surface, number 1, is also fixed to the footwall, but hanging-wall material appears to migrate through it as shortening continues (Figure 7B). Axial surfaces 2 and 3 immediately bound the fold crest, and are only recognized by discontinuities in the vertical

velocity field (Figure 7A). These surfaces move slightly and/or change orientation during continued shortening, suggesting they are loosely fixed to the hanging wall (Figure 7B). Throughout the first stage of deformation, the sand layers in the fold limbs rotate and experience some component of pure shear.

The end of the first deformation stage is marked by a short, transient stage of strain localization that precedes ramp overthrusting. In this particular experiment at a cumulative shortening of 4.2 mm, the deformation gradually focused along two discrete shear bands, each dipping approximately 25˚ toward the hinterland. Although the shear bands occur as prominent features in the horizontal displacement field (Figure 4B and 5B), they accommodate less than 30% of the total deformation. With continued shortening the more internal shear band, which approximately coincides with axial surface 3 defined in the vertical displacement field, tends to become dominant and evolves into a well-developed thrust fault connecting the basal décollement to the surface (Figures 4C and 5C). Formation of this frontal thrust ramp induces a significant change of model deformation kinematics and marks, then, the end of the fault tip stage.

At the beginning of the second stage of deformation, when the cumulative shortening typically exceeds about 6 mm, or roughly 13% of the initial thickness of the sand layers ($h/8$), a prominent thrust ramp exists at the front of the sand wedge (Figures 4C, 4D, 5C and 5D). The footwall subsequently stops deforming and all the horizontal shortening is taken up by slip on this shear zone, which acquires a stable sigmoid geometry. The hanging wall is then thrusted over the ramp with some internal deformation to accommodate the flat-to-ramp geometry. Axial surface 1 remains fixed to the footwall whereas axial surface 2 is fixed to the hanging wall and is passively transported along the fault. Thereafter, the velocity field remains constant, because the

fault geometry ceases to evolve. In general, the kinematics of the second stage of deformation is very similar to those of a simple ramp anticline as predicted by fault-bend folding theory [*Suppe* 1983] (Figure 2A).

Figure 8 shows how the maximum uplift rate, U_{max}, varies during a complete experiment. Before deformation gets localized, maximum uplift rate is observed to increase gradually and may be as large as twice the value predicted by fault-bend folding theory:

$$U_{max} = r \cdot \sin \theta_{max} \tag{3}$$

where r is the shortening rate and θ_{max} is the maximum dip angle of the fault, here about 25˚. This result is consistent with little internal deformation within the sand layers, and demonstrates that care must be taken when inferring shortening rates from uplift rates during the detachment-tip folding phase of deformation that is prior to the formation of the thrust ramp.

4. Analytical representations of surface uplift and horizontal velocity during fault-tip folding.

Vertical displacements are described from linear segments connecting the four axial surfaces (Figures 5 and 7). The axial surfaces are generally well defined from the profiles run at elevations above about 25 mm, but are generally more difficult to track closer to the décollement where vertical displacements are smaller. The geometry of the first axial surface is not always well determined since it extends outside the image. Horizontal displacements vary linearly with horizontal distance between two bounding axial surfaces (Figure 5).

During the first detachment-tip folding stage of deformation, we observe that horizontal velocity, V, decreases linearly with x, and tapers to zero at ~ 30 mm ahead of the axial surface 4 (Figure 4A and 5A). Incremental horizontal displacements can be described by

$$V = r(z) \cdot \left(1 - \lambda(z) \cdot x\right) \tag{4}$$

where $r(z)$ is the horizontal incremental shortening at the back of the structure and $\lambda(z) = 1/W_h(z)$, and $W_h(z)$ is the distance between axial surfaces 1 and 4.

Because the maximum uplift rate scales linearly with the initial datum elevation, z (Figure 9), we may write:

$$U_{max} = \gamma \cdot z + \mu \tag{5}$$

In the ideal case of a zero thickness décollement, the parameter μ should be equal to zero because no uplift would be observed at the level of the décollement. This parameter μ is not zero in our experiment because the décollement is a shear zone of finite thickness.

In addition, as shown in Figure 9, the uplift profile at each depth obeys

$$\frac{\Delta U / U_{max}}{\Delta X} = \eta \tag{6}$$

where ΔU is the difference in uplift at two points separated by a horizontal distance ΔX. Since U_{max} depends linearly on z, we get

$$\frac{\Delta U}{\Delta X} = \eta \cdot \left(\gamma \cdot z + \mu\right), \tag{7}$$

which implies that the pattern of incremental uplift in each dip domain between the axial surfaces can be written as

$$U = \eta \cdot \left(\gamma \cdot x \cdot z\right) + \mu \cdot x + \delta(z), \tag{8}$$

where the parameters $\eta, \gamma, \beta, \delta$ depend on the considered dip domain. This simple parameterization yields a good fit to the data (Figure 10). For easier use, equation (8) can be rewritten for each domain, i,

$$U(x,z) = U(x_i,z) + \alpha_i \cdot z \cdot (x - x_i)\,, \qquad (9)$$

where α_i is a constant parameter for each dip domain i considered; the term $U(x_i,z)$ corresponds to the vertical increment within the dip domain (i-1) at the horizontal position x_i of the axial surface shared by consecutive dip domains i and (i-1), and allows for continuity of vertical displacements from one dip domain to the next one. Since the surface area of the deforming domain is approximately constant, $U(x,z)$ depends uniquely on the parameters in equation (9) and on the position of the two axial surfaces defined from the horizontal displacements. The predicted horizontal velocity obtained from that assumption is in quite good agreement with the measurements (Figure 10A). During the transition from the initial stage of distributed deformation to ramp anticline formation, horizontal displacements need a more complex formulation. A reasonable fit to the data is however still obtained by assuming again mass conservation and linear functions between axial surfaces (Figure 10B).

5. Comparison with other models of fault-related folding

5.1 Comparison with an elastic dislocation model

We discuss first the possibility of modeling the observed kinematics from dislocations embedded in an elastic half-space [*Okada*, 1985]. Although the deformation observed in the experiment is not recoverable, hence non-elastic, it might be argued that this kind of model might provide a reasonable approximation to the velocity field [e.g., *Ward and Valensise*, 1994]. Following Ward and Valensise [1994] we have imposed a coefficient of Poisson of 0.5 to insure conservation of volume. We found it impossible to correctly predict simultaneously the vertical and horizontal velocities from this approach (Figures 11 and 12). We reached the same conclusion while analyzing the stage of fault-tip folding and the stage of ramp overthrusting. In

both cases, we find that slip rates derived from modeling the uplift pattern using elastic dislocations would be overestimated. It is generally possible to obtain a reasonable fit to the the profile of uplift rate at the surface, or in a naturale case to deformed seismic reflectors from this approach, , but inferences of fault geometry at depth and any displacement rates might be biased and should be considered with caution.

5.2 Comparison with trishear folding

The kinematics observed in our experiments show similarities with the trishear fault-propagation model [*Erslev*, 1991]. In the trishear model, a single fault expands outward into a triangular zone of distributed shear. An unlimited number of velocity fields and shapes of the triangular zone can be generated by varying the propagation-to-slip ratio (P/S), which determines how rapidly the tip line propagates relatively to the slip on the fault itself [*Allmendinger*, 1998; *Allmendinger and Shaw*, 2000; *Zehnder and Allmendinger*, 2000].

In the first phase results from distributed shear in a domain delimited by the two bounding hinges. Shear is not homogeneous and the deforming domain is not exactly triangular. As formulated in previous studies the trishear models requires in addition that the fault dip angle lies between the dip angles of the two boundaries of the triangular zone of distributed shear. As a result, it is not possible to model distributed shear above the tip of a décollement. Hence the model doesn't apply directly to the first phase. The trishear model might be adapted to that case but here we rather opted for the formulation described above (equation (4) and (9)) which ignores the propagation of the décollement.

Deformation during the stage of propagation of the frontal ramp propagation is close to a trishear fold mechanism although there is no clear indication in our experiment of propagation of the tip of the ramp during this transient stage of strain localization (Figure 2 B4).

5.3 Comparison with the fault-bend fold model

Once the frontal ramp has propagated up to the surface (when cumulative regional shortening exceeds $h/8$) the system evolves toward a ramp anticline. In this case, the uplift rate pattern is fully determined by the shortening rate, r, and the fault geometry, which controls the position of the axial surfaces. A possible kinematic model would be that the hanging wall deforms by bedding plane slip according to the fault-bend folding model [*Suppe,* 1983], which assumes the conservation of the length and thickness of the sand layers. Here, we test whether this model can be used to model the kinematics of folding in the stage of ramp-anticline folding. In such a case, equation (1) would hold as soon as the sand layers become parallel to the fault, as pictured in Figure 13, and hence when the cumulative slip on the ramp exceeds $U/\sin(\theta)$ (where θ is the average dip angle of the fault). In the hanging wall, uplift rate depends on the dip of the fault at depth, which is equal to the local bedding dip angle. If the fault dip angle is θ at the x' coordinate, at depth z the x coordinate where the bedding dip angle is θ, is $x = x' - z \cdot \tan(\theta)$ (Figure 13). The relation between the horizontal displacement $V(x)$ and the vertical displacement $U(x)$ is then simply,

$$V(x) = U(x) / \tan\theta(x') \tag{10}$$

where the fault dip angle $\theta(x')$ at point x' as defined above. To test the model, the fault shown on Figure 7C was determined from the measured strain field and adjusted from a fourth order polynomial. The measurements rather suggest a shear zone with a finite thickness of the order of

3 mm. In order to improve the fit of the model and avoid having large misfits near the fault zone (which could artificially increase the RMS between the data and the predicted displacements), the predicted displacements were smoothed with a gaussian function with a variance of 3 mm. We observe that this formulation provides a relatively good fit to the uplift rates, but the cumulative slip is less than the critical value, $U/\sin(\theta)$, (RMS of 10.9 10^{-3} mm/step between steps 150 and 153). If this model were used to estimate shortening rate from the measured uplift rate in the experiment, it would underestimate the actual value by 8-10 %. This shows that the ramp overthrusting stage of our experiment does not exactly obey the fault-bend fold model, which can be explained by the fact that beds near the surface are not yet parallel to the thrust fault at depth.

5.4 Comparison with a simple shear folding model

Another way to relate horizontal and vertical velocities along the profile after deformation gets localized is to assume that the hanging wall deforms by simple shear as pictured in Figure 14. This model obeys mass conservation only if the slip on the fault plane varies with the fault dip angle. Given that there is no length line change for lines parallel and perpendicular to the direction of simple shear, the projection of the velocity vector at any point in the direction perpendicular to the simple shear direction must be constant and equal to $r.\sin(\psi)$, where r is the shortening at the back of the structure, and ψ the simple shear angle defined in Figure 14. The slip r' on the fault is then expressed by :

$$r'(x) = \frac{r \cdot \sin\psi}{\sin(\psi - \theta(x))} \qquad (11)$$

where $\theta(x)$ is the local fault dip angle at point x.

The surface uplift at abscissa point x is then related to the uplift on the fault at a point x' with $x = x' + z(x') * \tan\psi$ (Figure 14). The local uplift at the x coordinate can therefore be written as

$$U(x) = r'(x') \cdot \sin\theta(x'), \tag{12}$$

with $\theta(x')$ the fault dip angle at point x', and $r'(x')$ the slip on the fault at the same point. Using (11) and (12), we can deduce the shortening r from the uplift profile,

$$r(x) = \frac{U(x) \cdot \sin(\psi - \theta(x'))}{\sin\psi \cdot \sin\theta(x')}. \tag{13}$$

Assuming simple shear deformation, the horizontal displacement $V(x)$ along the section is then related to the vertical displacement $U(x)$ and the fault dip angle at point x' according to

$$V(x) = \frac{U(x)}{\tan(\theta(x'))}, \tag{14}$$

where $\theta(x')$ is the fault dip angle at point x' as defined above.

This model predicts a sharp discontinuity of displacements across the fault which can lead to large local misfits when modeled and observed displacements are compared. To attenuated this effect, the displacements predicted from the model are smoothed with a gaussian function with a variance of 3 mm.

We have next varied the simple shear angle, ψ, in order to maximize the fit to the observed displacements. It turns out that the best fit is found for an angle of about 105° (Figure 15). This modeling provides an excellent fit to the data (RMS of 8.62 10^{-3} mm/step for the vertical velocities and rms of 16.95 10^{-3}mm/step for the horizontal velocities between steps 150 and 153) reconciling both vertical and horizontal velocities (Figure 16), except at the back of the structure, where the fault is almost horizontal. Because the best fitting shear angle does not exactly bisect the detachment and the ramp dip angle, this direction of shear implies changes of

the thickness and length of the sand layers during folding [*Suppe*, 1983]. Hanging-wall units consequently thicken during their transport above the ramp, as also observed in other experiments [*Maillot and Koyi,* 2006; *Koyi and Maillot,* 2006].

6. Discussion on the folding mechanism observed in the analogue experiment

In this experiment folding results primarily from distributed plastic shear. After a critical value of shortening ($h/8$), strain starts to localize and a frontal ramp develops. The ramp forms by strain localization close to a passive axial surface (the third one described above) where strain was able to accumulate during the first stage of folding (Figure 17). Because of this location the tilted forelimb formed earlier becomes part of the footwall once the ramp is formed. Memory of the initial phase of fault propagation is thus preserved in the footwall and in the hangingwall from the tilted forelimb. Note that in the presence of erosion, once the system has become a ramp anticline, the memory of the initial phase of deformation in the hanging wall would be lost but preserved in the footwall (Figure 17). Such a geometry has been observed across several piedmont folds north of the Tien Shan which were inferred to have evolved from fault-tip folds to fault-bend folds [*Avouac, et al.*, 1993].

Qualitatively, the behavior observed in this experiment is probably not specific to the particular setting of the experiment selected for this study. From a mechanical point of view, the axial surfaces are the expression of developing conjugate shear bands bounding a symmetrical pop-up structure (Figure 5B). After the localisation of the favoured fore-thrust shear zone (Figure 5C) back-thrust shear zone is moving as part of the hangingwall on the ramp. The detail of the kinematics, however, must depend highly on the particular geometrical set-up and material properties in the selected experiment. For example, it is probable that the amount of distributed

deformation reached before localization is related to the onset of strain hardening and probably depends on factors such as the grain size and compaction [*Lohrmann, et al.*, 2003]. A complete mechanical analysis of the observed kinematics is beyond the scope of this study and would require a parametric study to elucidate the influence of each of the governing material properties and of the geometry (dependence on layer thickness, dependence on layering, etc.).

During ramp overthrusting, we find a good fit between observed incremental displacements and the simple-shear model assuming an optimal simple-shear angle of 105º (ψ in Figure 14). Most of the shear occurs in the area where the detachment connects with the ramp. This zone thus appears as a migrating kink band, equivalent to a transient backthrust dipping by 65 º. Maillot and Leroy [2003] have determined the optimal dip of the backthrust in such a fault-bend fold that would correspond to a minimum of dissipated energy within the whole structure. The three sources of dissipation are due to frictional sliding on the ramp, on the backthrust and on the décollement [*Maillot and Leroy,* 2003]. As mentioned above, the basal coefficient of friction is estimated to 21° in this experiment. According to Maillot and Leroy [2003], the optimal dip of the back thrust would be 30° in this case, which implies a simple shear angle of 150° quite different from that observed in the experiment. The system does not seem to respond as expected from the minimization of total dissipation. The observed kinematics does not conform either to the kinematics expected from conventional fault-bend folding [*Suppe*, 1983]. This is because, despite the presence of the glass beads layers, layer-parallel longitudinal strain dominates over layer-parallel shear in this experiment.

7. Guidelines for the analysis of natural fault-tip folds.

We outline here how the fault-tip fold kinematic model described above can be used to analyze natural folds. It is first assumed here that cross sectional area is preserved during folding. It should be recalled that a variety of mechanisms can lead to volume changes in analogue models, as observed in our experiment, or at the scale of natural folds such as tectonic compaction, dilatancy, or pressure solution, [*Koyi*, 1995; *Marone*, 1998; *Whitaker and Bartholomew,* 1999; *Lohrmann, et al.,* 2003; *Koyi and Cotton,* 2004; *Adam*, 2005]. The approach assumes in addition that the deformation field is stationary, meaning that all the axial surfaces remain fixed relative to the undeformed footwall. This is only a first order approximation (Figure 7). Provided that these assumptions are correct, the analytic model makes it possible to retrieve the history of shortening across a fold from growth strata or from deformed fluvial terraces [*Simoes, et al.*, this issue; *Daeron, et al.*, this issue]. First, the analytical expressions need to be calibrated based on the finite geometry of the fold, (as images by seismic profiles for example). As an illustrationand to test the hypothesis that deformation can be assumed stationnary, we use the finite geometry after 3.4 mm of horizontal shortening, when localization of the fault has initiated at depth (Figure 18).

7.1 Relating dip-angle and shortening for fault-tip folds.

The key observation in the experiment is that uplift rate varies linearly within domains separated by axial surfaces (equation (9)), whereas incremental horizontal displacement varies linearly with a constant gradient over the whole fold area (equation (4)). The change in dip angle associated with an incremental shortening r, within a certain domain i is then given by

$$\tan(\beta) = \frac{\alpha_i \cdot z \cdot r}{1 - \lambda(z) \cdot r} \quad (15)$$

where β is the dip acquired after an incremental shortening *r*, in the case of a growth or a pre-growth stratum. This relation can thus be used to infer the cumulative shortening recorded by tilted structural horizons or geomorphic surfaces, and if a set of pre-growth and growth strata are available, the history of folding can be retrieved.

To calibrate the fold model parameters, the finite structure of the fold is used. Within each domain *i*, the coefficients in equation (15) might be determined from the observed structural dip angles of pre-growth strata (equivalent to β in equation (15)) provided that the cumulative shortening (equivalent to *r*) and depth to the décollement (*z*) are known. In practice, these latter two can be estimated from the excess area method [*Chamberlin*, 1910; *Epard and Groshong*, 1993]. Conservation of mass implies that the area *A* below a deformed level at an initial altitude *z* above the décollement equals the product $z \cdot R$, where *R* is the average total shortening of the layers below the considered horizon (Figure 1). By plotting *A* vs. *z*, one should obtain a linear relationship constraining both the cumulative shortening *R* and the depth to the décollement *z* (Figure 19). In the case of our analogue experiment, the retrieved plot is approximately linear but does not meet the condition that the excess area should be zero at the decollement (Figure 19). If the depth of the decollement was not known independently we would underestimate the décollement depth, and overestimate shortening by 55% (5.3 mm instead of 3.4 mm). This is a problem that has also been noticed in natural examples [*Scharer, et al.*, 2004, *Simoes, et al.*, this issue], and décollement parallel shear back of the fold, sometimes termed 'backshear', was advocated as a possible explanation. If backshear is assumed constant with depth, the function describing how the excess area varies with depth is parabolic (Figure 19A). In our case, a parabolic curve doesn't improve much the fit to the data and neither yield the right estimate of *R*.

In fact, this explanation doesn't since the horizontal velocity field show no evidence for backshear. The discrepancy rather relates to the fact that the cross-sectional area is not conserved during the phase of fault-tip folding. If we now impose the décollement depth by forcing the linear regression through the origin of the axis (A=0 at z=0), the excess-area approach yields a total shortening of 3.6 mm close to the known experimental value. It therefore turns out that an independent constraint on the décollement depth is preferable when applying the excess area method to fault-tip folds and that, without such information, the estimated shortening and décollement depth could be biased.

7.2 Determination of λ and α_i describing incremental displacements.

Once axial surfaces are defined, $\lambda(z)$ may be easily determined from the width of the fold, $W_h(z)$, measured at several elevations above the décollement, z. Given the estimated depth to the décollement, the value of α_i in each dip domain i can then be calculated from equation (15) (Figure 20).

With these parameters, the synthetic fold geometry is reasonably well adjusted by the model (figure 21). Mismatches most likely result from the fact that we did not allow for migration of fold axial surfaces over time, and that at the stage of fold development chosen for this test, strain localization has already begun. Also, the model parameters have been calibrated from the finite structure, assuming a stationary deformatiom field.

7.3 Testing the model against incremental deformation

The model calibrated from the analysis of the finite structure can be used to predict vertical and horizontal incremental displacements. It turns out that they compare relatively well

with the incremental displacements measured from the analogue experiment itself, except for the most frontal zone where shear bands and compaction are observed at this advanced stage of fault-tip-folding (Figure 21). Excluding this domain, the observed discrepancy is within 10% of the incremental shortening imposed at the back of the fold, and it appears that the model usually tends to slightly underestimate the actual incremental deformation. The model derived from the finite structure seems thus adequate to describe the incremental growth of the fold, even at this advanced stage of fault-tip folding. This validates the idea that incremental uplift or limb tilt that is recorded from terraces or growth strata can be analyzed from such simple analytical formulations to derive corresponding horizontal incremental shortening.

8. Conclusion

The experiment analyzed in this paper mimics the development of a fold growing over a propagating basal décollement which evolves towards a ramp-anticline. In the early stage, deformation is distributed leading to thickening and shortening of the sand layers. This mechanism results in gradual tilting of the forelimb and backlimb. Up to about $h/8$ of shortening, deformation of the medium is distributed and the fold grows as a result of thickening and shortening of the sand layers leading to limb rotation. Our measurements suggest that the fold kinematics can be described from a simple analytical formulation, which assumes that the velocity field is a linear function of depth and horizontal distance. Most importantly, the gradient of horizontal displacements is constant across the whole fold zone as long as strain does not localize. Once deformation is localized, a stable frontal ramp is formed and the system behaves as a ramp anticline. During this stage of deformation the measured displacements can be

reproduced reasonably well assuming bed-parallel simple shear, as in the fault-bend fold model, or simple-shear parallel to a constant direction. We have observed the same qualitative behavior in other experiments similar to the one analyzed in detail in this study so that we can confidently state that the process described here is general, but we are unable at this point to assess how the observed kinematics relate to the mechanical properties of the sand and glass beads layers, or to the geometry of the experimental setup.

Based on the kinematic model derived from this experiment, we propose some procedure to retrieve the fold kinematics from growth strata geometry or deformed geomorphic markers. This approach has been applied successfully to the analysis of the Pakuashan anticline, west central Taiwan [*Simoes, et al.*, this issue] and to detachment folds along the piedmonts the Tien Shan [*Daeron, et al*., this issue].

Acknowledgments: We are grateful to Remi Michel for help in the design of the optical monitoring system. We also thank Jacques Malavieille, Rick Allmendiger and John Suppe for fruitful discussions. The manuscript has benefited from thorough reviews and helpful suggestions by Hemin Koyi, Jurgen Adam, Mark Fisher and the Associate Editor Wouter Schellart.

References

Adam, J., J. Urai, B., Wieneke, O. Oncken, K. Pfeiffer, N. Kukowski, J. Lohrmann, S. Hoth, W. van der Zee, and J. Schmatz, J. (2005), Shear localisation and strain distribution during tectonic faulting--new insights from granular-flow experiments and high-resolution optical image correlation techniques, *Journal of Structural Geology, 27*(2), 283--301.

Allmendinger, R.W. (1998), Inverse and forward numerical modeling of trishear fault-propagation folds, *Tectonics 17*(4), 640--656.

Allmendinger, R.W. and J.H. Shaw (2000), Estimation of fault propagation distance from fold shape: Implications for earthquake hazard assessment, *Geology 28*(12), 1099--1102.

Avouac, J. P., P. Tapponier, M. Bai, H. You and G. Wang (1993), Active thrusting and folding along the Northern Tien-Shan and Late Cenozoic Rotation of the Tarim Relative to Dzungaria and Kazakhstan, *Journal of Geophysical Research – Solid Earth, 98*(B4), 6755—6804.

Brooks, B.A., E. Sandvol, and A. Ross (2000), Fold style inversion: Placing probabilistic constraints on the predicted shape of blind thrust faults, *Journal of Geophysical Research – Solid Earth, 105*(B6), 13281--13301.

Burbank, D., and R. Anderson (2001) *Tectonic geomorphology*, p. 274, Blackwell Science, Malden, MA.

Chamberlin, R.T. (1910), 'The Appalachian folds of central Pennsylvania', *Journal of Geology, 27*, 228--251.

Chapple, W.M. (1978), Mechanics of thin-skinned fold-and-thrust belts, *Geological Society of America Bulletin, 89*(8), 1189--1198.

Daeron, M., J.P. Avouac, J. Charreau, and S. Dominguez, Modeling the shortening history of a fault-tip fold using structural and geomorphic records of deformation, *Journal of Geophysical Research*, *this issue*.

Dahlstrom, C.D.A. (1990), Geometric constraints derived from the law of conservation of volume and applied to evolutionary models for detachment folding, *AAPG Bulletin-American Association of Petroleum Geologists, 74*(3), 336--344.

Davis, D., J. Suppe, and F.A. Dahlen (1983), Mechanics of fold-and-thrust belts and accretionary wedges, *Journal of Geophysical Research, 88*(NB2), 1153--1172.

Dominguez S., J. Malavieille and S.E. Lallemand (2000). Deformation of margins in response to seamount subduction - insights from sandbox experiments; *Tectonics*, *19*, n°1, 182-196.

Dominguez S., R. Michel, J.P. Avouac, and J. Malavieille (2001). Kinematics of thrust fault propagation, Insight from video processing techniques applied to experimental modeling, EGS XXVI, Nice, March 2001.

Dominguez, S., J. Malavieille, and J.P. Avouac (2003), Fluvial terraces deformation induced by thrust faulting : an experimental approach to better estimate crustal shortening velocities. EGS-AGU-EUG Joint Assembly, Nice, Abstract number EAE03-A-11321

Epard, J.L., and R.H. Groshong (1993), Excess area and depth to detachment, *AAPG Bulletin-American Association of Petroleum Geologists, 77*(8), 1291--1302.

Epard, J.L., and R.H. Groshong (1995), Kinematic model of detachment folding including limb rotation, fixed hinges and layer-parallel strain, *Tectonophysics, 247*(1-4), 85--103.

Erslev, E.A. (1991), Trishear fault-propagation folding, *Geology 19*(6), 617--620.

Gutscher, M.A., N. Kukowski, J. Malavieille, and S. Lallemand (1998), Material transfer in accretionary wedges from analysis of a systematic series of analog experiments, *Journal of Structural Geology, 20*(4), 407--416.

Hardy, S., and J. Poblet (1994), Geometric and numerical-model of progressive limb rotation in detachment folds, *Geology, 22*(4), 371--374.

Hardy, S., J. Poblet, K. McClay, and D. Waltham (1996), Mathematical modelling of growth strata associated with fault-related fold structures, *Special Publication Geological Society*, *99*, 265--282.

Horn, B.K.P., and B.G. Schunck (1980), Determining optical flow, *Technical Report A.I. Memo 572*, Massachusetts Institute of Technology.

Jolivet, M. (2000), Cinématique des déformations au Nord Tibet. Thermochronologie, traces de fission, modélisation analogique et études de terrain, *Thesis, Université Montpellier II.*

King, G.C.P., R.S. Stein, and J.B. Rundle (1988), The growth of geological structures by repeated earthquakes. 1. Conceptual-framework, *Journal of Geophysical Research –Solid Earth and Planets, 93*(B11), 13307--13318.

Konstantinovskaia, E., and J. Malavieille (2005), Erosion and exhumation in accretionary orogens: Experimental and geological approaches, *Geochemistry Geophysics Geosystems 6*, Q02006, doi:10.1029/2004GC000794, ISSN: 1525-2027.

Koyi, H. (1995), Mode of internal deformation in sand wedges, *Journal of Structural Geology, 17*(2), 293--300.

Koyi H. A., and J. Cotton (2004) Experimental insights on the geometry and kinematics of fold-and-thrust belts above weak, viscous evaporitic decollement; a discussion, *Journal of Structural*

Geology, 26(11), 2139--2141

Koyi, H. and B. Maillot (2006), The effect of ramp dip and friction on thickness change of hangingwall units; a necessary improvement to kinematic models, paper presented at the annual general meeting of the Tectonic Studies Group of the Geological Society of London, Manchester England.

Krantz, R.W. (1991), Measurements of friction coefficients and cohesion for faulting and fault reactivation in laboratory models using sand and sand mixtures, *Tectonophysics*, *188*(1-2), 203--207.

Lohrmann, J., N. Kukowski, J. Adam, and O. Oncken (2003), The impact of analogue material properties on the geometry, kinematics, and dynamics of convergent sand wedges, *Journal of Structural Geology*, *25*, 1691--1711.

Lallemand, S.E., P. Schnurle, and J. Malavieille (1994), Coulomb theory applied to accretionary and nanoaccretionary wedges – Possible causes for tectonic erosion and or frontal accretion, *Journal of Geophysical Research – Solid Earth, 99*(B6), 12033--12055.

Lavé, J., and J.P. Avouac (2000), Active folding of fluvial terraces across the Siwaliks Hills, Himalayas of central Nepal, *Journal of Geophysical Research - Solid Earth, 105*(B3), 5735--5770.

Maillot, B., and Y.M. Leroy (2003), Optimal dip based on dissipation of backthrusts and hinges in fold-and-thrust belts, *Journal of Geophysical Research, 108* (B6), 2320--2339.

Maillot, B., and H. Koyi (2006), Thrust dip and thrust refraction in fault-bend folds: analogue models and theoretical predictions, *Journal of Structural Geology, 28*(1), 36--49.

Malavieille, J. (1984). Modélisation expérimentale des chevauchements imbriqués : application aux chaînes de montagnes, *Bulletin de la Société géologique de France*, *XXVI*(1), 129--138.

Marone, C. (1998), Laboratory-derived friction laws and their application to seismic faulting, *Annual Review of Earth and Planetary Sciences*, *26*, 643—696.

Medwedeff, D.A., and J. Suppe (1997), Multibend fault-bend folding, *Journal of Structural Geology, 19*(3-4), 279--292.

Mitra, S. (2003), A unified kinematic model for the evolution of detachment folds, *Journal of Structural Geology, 25*(10), 1659--1673.

Molnar, P., E.T. Brown, B.C. Burchfiel, D. Qidong, F. Xianyue, L. Jun, G.M. Raisbeck, S. Jianbang, W. Zhangming, F. Yiou, and Y. Huichuan (1994), Quaternary climate-change and the formation of river terraces across growing anticlines on the north flank of the Tien-Shan, China, *Journal of Geology, 102*(5), 583--602.

Mosar, J., and J. Suppe (1992), Role of shear in fault-propagation folding., in *Thrust tectonics.*, edited by K. R. McClay, pp. 123--132, Chapman & Hall, London, United Kingdom (GBR).

Mulugeta, G. (1988), Squeeze Box in a centrifuge, *Tectonophysics, 148*(3-4), 323--335.

Mulugeta, G., and H. Koyi (1992), Episodic accretion and strain partitioning in a model sand wedge, *Tectonophysics, 202*(2-4), 319--333

Myers, W. B., and W. Hamilton (1964), Deformation accompanying the Hebgen Lake Earthquake of August 17, 1959, in *The Hebgen Lake, Montana, Earthquake of August 17, 1959*, U.S. Geol. Surv. Prof. Pap, 435, 55--98.

Okada, Y. (1985), Surface deformation due to shear and tensile faults in a half-space, *Bulletin of the Seismological Society of America, 75*(4), 1135--1154.

Poblet, J., and K. McClay (1996), Geometry and kinematics of single-layer detachment folds, *AAPG Bulletin-American Association of Petroleum Geologists, 80*(7), 1085--1109.

Press, W. H., S.A. Teukolsky, W.T. Vetterling, and B.P. Flannery, (1995), *Numerical Recipes in C: The Art of Scientific Computing (Hardcover)*, Cambridge University Press.

Rockwell, T.K., E.A. Keller, and G.R. Dembroff (1988), Quaternary rate of folding of the Ventura Avenue anticline, Western Transverse Ranges, Southern California, *Geological Society of America Bulletin, 100*(6), 850--858.

Savage, H.M., and M.L. Cooke (2004), The effect of non-parallel thrust fault interaction on fold patterns, *Journal of Structural Geology, 26*(5), 905--917.

Scharer, K.M., D.W. Burbank, J. Chen, R.J. Weldon, C. Rubin, R. Zhao, and J. Shen (2004), Detachment folding in the Southwestern Tian Shan-Tarim foreland, China: shortening estimates and rates, *Journal of Structural Geology, 26*(11), 2119--2137.

Schellart, W.P. (2000), Shear test results for cohesion and friction coefficients for different granular materials: scaling implications for their usage in analogue modelling, *Tectonophysics, 324*(1-2), 1--16.

Simoes, M., J.P. Avouac, Y-G. Chen, A.K. Singhvi, C-Y. Wang, M. Jaiswal, Y-C. Chan, and S. Bernard, Kinematic analysis of the Pakuashan fault-tip fold, West Central Taiwan: shortening rates and age of folding inception, *Journal of Geophysical Research-Solid Earth*, this issue.

Stein, R.S., G.C.P. King, and J.B Rundle (1988), The growth of geological structures by repeated earthquakes. 2.Fiel examples of continental dip-slip faults, *Journal of Geophysical Research - Solid Earth and Planets, 93*(B11), 13319--13331.

Storti, F., and J. Poblet (1997), Growth stratal architectures associated to décollement folds and fault-propagation folds. Inferences on fold kinematics, *Tectonophysics, 282*(1-4), 353--373.

Suppe, J. (1983), Geometry and kinematics of fault-bend folding, *American Journal of Science, 283*(7), 684--721.

Suppe, J., and D.A. Medwedeff (1990), Geometry and kinematics of fault-propagation folding, *Eclogae Geologicae Helvetiae, 83*(3), 409--454.

Suppe, J., G.T. Chou, and S.C. Hook (1992), Rates of folding and faulting determined from growth strata, in *Thrust Tectonics*, edited by K. R. McClay, pp. 105--121, Chapman and Hall, New York.

Thompson, S.C., R.J. Weldon, C.M. Rubin, K. Abdrakhmatov, P. Molnar, and G.W. Berger (2002), Late Quaternary slip rates across the central Tien Shan, Kyrgyzstan, central Asia, *Journal of Geophysical Research - Solid Earth, 107*(B9), 2203.

Van der Woerd, J., X.W. Xu, H.B. Li, P. Tapponnier, B. Meyer, F.J. Ryerson, A.S. Meriaux, and Z.Q. Xu (2001), Rapid active thrusting along the northwestern range front of the Tanghe Nan Shan (western Gansu, China), *Journal of Geophysical Research - Solid Earth, 106*(B12), 30475--30504.

Ward, S.N., and G. Valensise (1994), The paleo-verdes terraces, California – Bathtub rings from a buried reverse-fault, *Journal of Geophysical Research - Solid Earth, 99*(B3), 4485--4494.

Whitaker, A. E., and M. J. Bartholomew (1999), Layer parallel shortening: A mechanism for determining deformation timing at the junction of the central and southern Appalachians, *American Journal of Science, 299*(3), 238-254.

Wickham, J. (1995), Fault displacement-gradient folds and the structure at Lost-Hills, California (USA), *Journal of Structural Geology, 17*(9), 1293--1302.

Zehnder, A.T., and R.W. Allmendinger (2000), Velocity field for the Trishear model, *Journal of Structural Geology, 22*(8), 1009--1014.

Table

Table 1 : List and definition of the variables introduced in the analysis.

Figure captions

Figure 1: A. Structure of a mature fault-tip fold. B. Continuous profile of a deformed terrace across the fold can be used to measure incremental folding. The area A defined by the deformed terrace above its initial geometry may be related to the total displaced area at the back of the fold since the terrace was abandoned (A) C. Sine of bedding dip angle along structural section, as for use in equation (1). It might be appropriate to perform such analysis to retrieve incremental deformation within the backlimb of the fault-tip fold represented, since it appears to be more mature in this portion of the fold, but may lead to large errors at the front where the structure is not mature enough and appears more complex.

Figure 2: Classification of fold models with emphasis on the kinematic record provided by the architecture of growth strata [*Burbank and Anderson*, 2001]. A- fault-bend folding [*Suppe*, 1983; *Medwedeff and Suppe*, 1997] results from the transfer of slip from a deeper to a shallower stratigraphic detachment level. The model assumes conservation of bed thickness and length during deformation. The hanging wall deforms by bed-parallel simple shear and axial surface migration. This model applies to mature faults, with a cumulative slip larger than the distance from the décollement to the surface (measured along the fault). B Various possible geometries of folds formed at the tip of a blind thrust fault. The fault-propagation fold model (B1) assumes conservation of bed length and thickness [*Suppe and Medwedeff*, 1990; *Mosar and Suppe*, 1992]. The slip gradient model (B2) does not require fault propagation. It assumes conservation of area but not of bed length [*Wickham*, 1995]. Model B3 assumes a changing bed length and forelimb angle [*Dahlstrom*, 1990; *Epard and Groshong*, 1995; *Mitra*, 2003]. Model B4 assumes a triangular shaped zone of distributed shear [*Erslev*, 1991; *Allmendinger*, 1998]. The choice of the appropriate model to use in the analysis of a natural case example is not straightforward.

Figure 3: (A) Experimental set-up. To build the model, granular materials were sprinkled into a 20 cm wide and 100 cm long box equipped with transparent side walls, similar to the experimental set-up used by Dominguez et al. [2000]. The sand layers slide on a horizontal (β=0) basal polyvinyl chloride (PVC) plate, 2 cm thick. Initially undeformed sand mass is compressed and deformed by a backstop moved by a step motor. A CCD camera takes pictures (6.3 Mpixels with a spatial resolution of 0.04 m^2) with a constant time step corresponding to 0.2 mm (equivalent to 2.7 pixel) of shortening between two successive images. (B) Initial conditions. Five low frictions glass bead layers are interlayered with the sand layers. (C) Summary of the optical flow technique for measuring displacements. The numerical video image at step 122 is compared to the one at step 120. The displacement field is computed from the optical flow technique as described in the text. The incremental displacement field is represented by vectors or a deformed grid. Also shown is the second invariant of the strain tensor ($I_2 = {}^1/_2[tr(\varepsilon)^2-tr(\varepsilon^2)]$ where ε is the deformation tensor), in gray scale to emphasize zones of strain localization

Figure 4: Incremental displacement field and strain measured during the stage of detachment-tip folding (between steps 05 and 08, cumulative shortening = 1 mm), the transitional stage of strain localization (between steps 20 and 23, cumulative shortening = 4.2 mm), and the stage of ramp overthrusting (between steps 80 and 83, cumulative shortening = 17 mm and between steps 200 and 203, cumulative shortening = 42.6 mm). For each of these plots the cumulative horizontal shortening is indicated. Note that in the early stage, deformation is not localized. After a cumulative shortening of about 6 mm it localizes on a frontal ramp connecting the basal décollement with the surface.

Figure 5: Horizontal and vertical displacement rates measured along profiles run at different depths during (A) the detachment-tip folding stage (between steps 10 and 12, cumulative shortening = 2.1 mm), (B) the transitional stage of strain localization (between steps 20 and 23, cumulative shortening = 4.2 mm) and (C and D) the stage of ramp overthrusting between steps 50 and 53 (cumulative shortening = 10.6 mm) and between steps 150 and 153 (cumulative shortening = 32 mm). The abscissa axis is positioned at the depth at which each profile is run.

Figure 6: Uplift rates during the detachment-tip folding stage (between steps 10 and 12), measured along profiles at different depths. For each profile, the position of the ordinate axis indicates the depth at which the profile is examined. The position of the various axial surfaces determined from the break-in-slope (circles) is indicated, as well as the locus of the maximum uplift rate on each profile (dark line). The first, second and third axial surfaces are reasonably well fit by a straight line suggesting a linear dependency with depth. A straight line also fits reasonably well the abscissa corresponding to the maximum uplift rates on each profile. The most frontal axial surface can be adjusted with a second order polynomial.

Figure 7: (A) Schematic pattern of uplift rates and horizontal velocities at various depths. As deformation increases, the positions of the axial surfaces evolve, in particular axial surfaces 3 and 4 nearly coalesce to define a localized shear zone corresponding to the frontal ramp. (B) Location of the three frontal axial surfaces during the experiment. (C) Geometry of the frontal

fault which forms after about 6 mm of shortening together with the positions of the axial surfaces determined from the vertical displacements.

Figure 8: Maximum uplift rate (at z = 50 mm) as a function of cumulative shortening. In the early stage of the experiment, during the stage of detachment-tip folding and the transitional stage of strain localization, before deformation gets strongly localized, the maximum uplift rate increases gradually. Once deformation is localized on a frontal ramp the maximum uplift rate is independent of the cumulative shortening and is simply $U_{max} = r * \sin\theta_{max}$ where r is the shortening rate and θ_{max} is the maximum dip angle of the fault, about 25°.

Figure 9: (A) Maximum uplift rates as a function of elevation above the décollement during the stage of detachment-tip folding (values from steps 10-12). A linear function (dashed line), as proposed in equation (5), provides a good fit (B) Normalized uplift rates at several depths. Uplift rates are normalized by the value of the maximum at each depth (values from steps 10-12).

Figure 10: Comparison of the measured displacements (blue dots) before fault localization during the detachment-tip folding stage (between steps 10 and 12) (A), and transitional stage of strain localization (between steps 20 and 23) (B) (ie for a cumulative shortening lower than 6 mm), and those predicted from the linear model detailed in text (red or green continuous lines). The rms of the fit to the uplift rate is 0.012103 mm/step between steps 10 and 12 (computed for the profile at an elevation of 50 mm above the décollement). The fit to the horizontal velocities yields a rms of 0.021771 mm/step between steps 10 and 12.

Figure 11: Results from dislocation modeling of observed vertical and horizontal velocities during the stage of detachment-tip folding, phase of fault-tip folding (between steps 10 and 12), using the theory of a dislocation in a elastic half space [*Okada*, 1985]. (Top left) Measured (blue) and modeled (black) vertical displacement at the surface. (Top right) Horizontal displacements extracted from the data (red) and calculated (lack). (Bottom left) Shape of the fault used to calculate displacement. (Bottom right) Value of the root mean square difference between observed and calculated vertical displacement as a function of slip rate on the décollement.

Figure 12: Results from dislocation modeling of observed vertical and horizontal velocities during the stage of ramp overthrusting (between steps 150 and 153). (Top left) Vertical displacement at the surface extracted from the data (blue) and calculated (black). (Top right) Horizontal displacements extracted from the data (red) and calculated (black). (Bottom left) Shape of the fault used to calculate displacement. (Bottom right) Value of the square difference between observed and calculated vertical displacement vs the fault slip.

Figure 13: Diagram showing how the incremental uplift, u, of an initially horizontal horizon relates to incremental shortening in the case of a mature fault-bend fold. The model assumes conservation of bed thickness and bed length and the hanging wall deforms only by bed-parallel shear. Uplift is proportional to the sine of the fault dip angle, equivalent to the local bedding dip angle, θ, and to the slip along the fault (equation (1)). The assumption of a constant bed thickness and length during deformation requires that at point with abscissa x at the surface the bedding dip angle equals the fault dip angle at the point with abscissa x' along the fault.

Figure 14: Sketch showing the relation between incremental shortening *r* and uplift of an initially horizontal horizon in the case of a ramp anticline with simple shear deformation of the hanging wall (simple shear angle ψ). Conservation of area implies that slip has to vary along the fault.

Figure 15: Plot showing how a model of ramp overthrusting with simple shear deformation of the hanging wall fits the observed uplift rates when the simple shear angle is varied (see sketch Figure 14). The best fitting shear angle is 104°. This result holds for all incremental displacements during this kinematic stage.

Figure 16: Comparison between observed horizontal and vertical velocities (blue dots) and the theoretical profiles (red or green continuous lines) predicted from ramp overthrusting with simple shear deformation of the hanging wall for a shear angle of 105º as sketched in Figure 15. See text for details.

Figure 17: Finite deformation of layers initially horizontal computed from the proposed analytical approximation to the measured displacement fields. Horizontal and vertical displacements are exaggerated by a factor of 8 for readability. At each stage the cross-section is obtained by applying incremental deformation to the previous stage. Erosion is not simulated, but displacements above the deformed surface after the first incremental shortening (0.2 mm) have not been modeled. The first 2 mm of shortening are not taken into account in this modeling. This choice implies a fault initiation after only 4 mm of shortening instead of 6 mm as discussed

in the text. The phase of fault-tip folding, up to 2.125 mm of shortening, assumes a stationary velocity field equivalent to that defined from steps 10 to 12 in the experiment. This corresponds to the phase of fault-tip folding. The fold structure for a shortening of 2.75 and 3.4 mm, corresponding to the transitional stage of strain localization, was obtained from the velocity fields derived from steps 20 to 23 at the onset of strain localization within the sand layers. Above 4 mm of shortening we assume ramp overthrusting with simple shear deformation of the hanging wall as observed in the experiment from steps 50 to 53 (stage of ramp overthrusting).

Figure 18: Structure of the modeled fold after an actual shortening of 3.4 mm corresponding to Figure 17. The geometry of the fold is not exaggerated here. The backlimb has been extrapolated slightly outside the zone covered by our measurements. Each colored surface corresponds to the fold core area (or 'excess area') above the initial elevation of the considered strata. Inclined lines indicate axial surfaces delimiting domains of homogeneous finite dips as determined from this finite structure.

Figure 19: Excess-area as a function of elevation above the décollement.(A) In the absence of any backshear excess area, A, varies linearly with elevation above the décollement following Chamberlin's law [*Chamberlin*, 1910]. In case of backshear the relationship is no more linear. (B) Variations of excess area, as derived from Figure 18, as a function of elevation. A simple linear regression through the data yields a finite shortening of 5.3 mm too high, and a décollement level too shallow. If the regression is forced through the origin to account for the known décollement, the estimated total shortening is close to the real value of 3.4 mm.

Figure 20: Parameters of the analytical formulations derived from the finite structure of the synthetic fold.(a) λ as a function of depth. (b) α_i for each one of the three domains

Figure 21: Computing the misfits between the observed the modeled fold kinematics. Residuals correspond to predicted minus observed dips or displacements. A- Distribution of the computed residuals in the dip angles between predicted and observed finite structures. Standard deviation and median are also reported. The highest residuals are observed in the vicinity of the axial surface lines. B- Residuals between predicted and observed horizontal incremental displacements for a total incremental displacement of 1mm at the back of the system. Most of the misfits occur around the shear bands that develop essentially at the front of the fold during steps corresponding to a cumulative shortening of 2.75 mm and 3.4 mm of Figure 18. Except for this area where deformation is underestimated by the model, the predicted horizontal displacements are in good agreement with the observed ones, within 10% of the applied displacement at the back of the system C- Residuals between predicted and observed vertical incremental displacements for a total incremental displacement of 1mm at the back of the system. Most of the underestimation of vertical incremental deformation results also from the influence of the shear bands at the front of the fold. As previously, the model is able to predict correctly the incremental displacements within 10% of the shortening applied at the back of the system.

Variable	Definition
h	Total thickness of the layers
ϕ	Measured basal friction angle
ϕ_b	Theoritical basal friction angle
ϕ_s	Internal friction angle of the sand mass
ϕ_g	Internal friction angle of the glass beads
U	Local uplift relative to the footwall
V	Horizontal shortening
x	Horizontal coordinate
z	Vertical coordinate
$\theta(x)$	Local dip angle
U_{max}	Maximum uplift rate
r	Shortening rate
θ_{max}	Maximum dip angle of the fault
λ	Horizontal displacement gradient
α_i	Vertical displacement gradient
ψ	Simple shear angle
r'	Slip on the fault in case of simple shear
β	Acquired dip due to an incremental shortening

Table 1

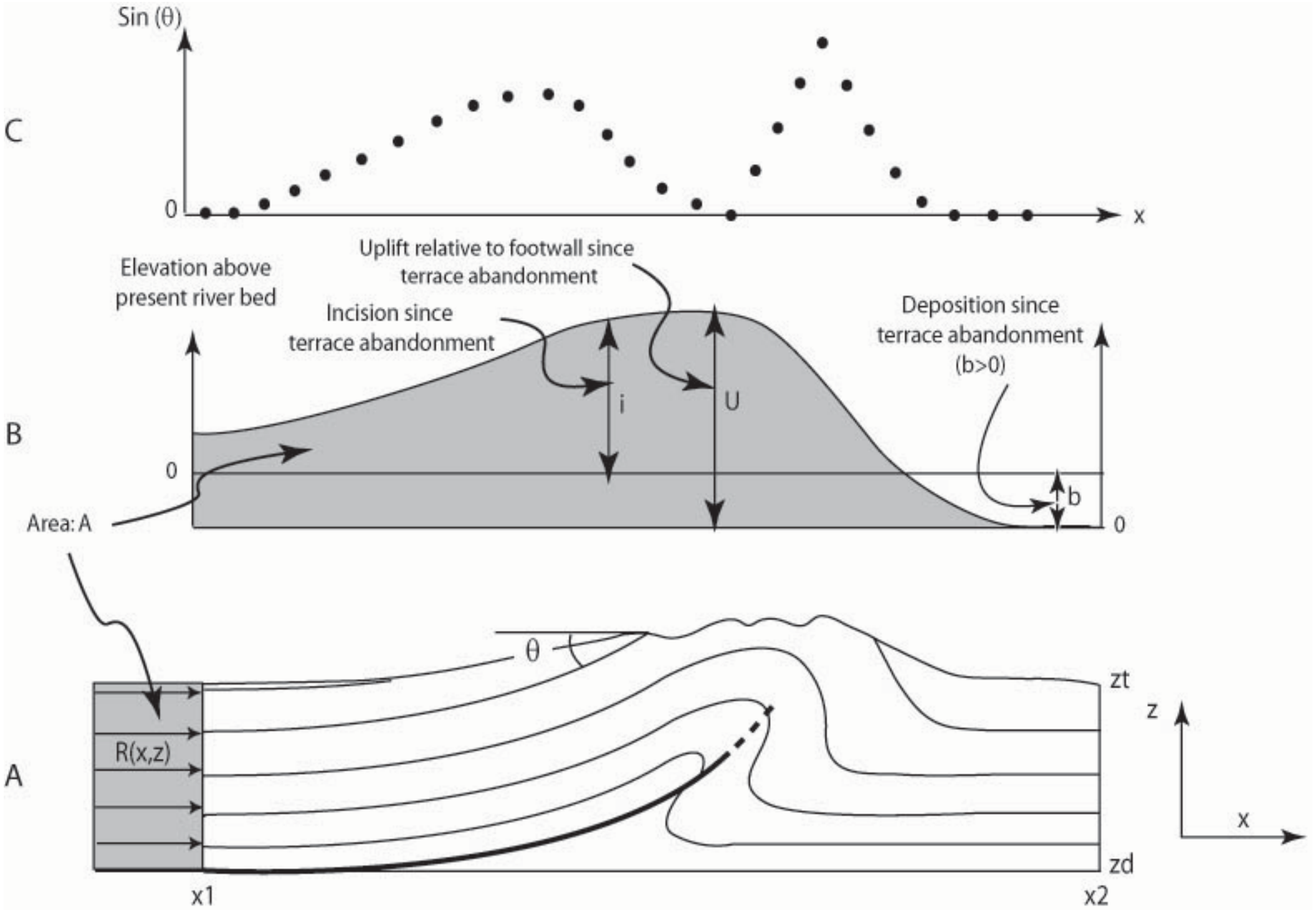
C
Sin (θ)
0
x
B
Elevation above
present river bed
Uplift relative to footwall since
terrace abandonment
Incision since
terrace abandonment
Deposition since
terrace abandonment
(b>0)
i
U
b
0
0
Area: A
A
R(x,z)
θ
zt
zd
z
x
x1
x2

figure 1

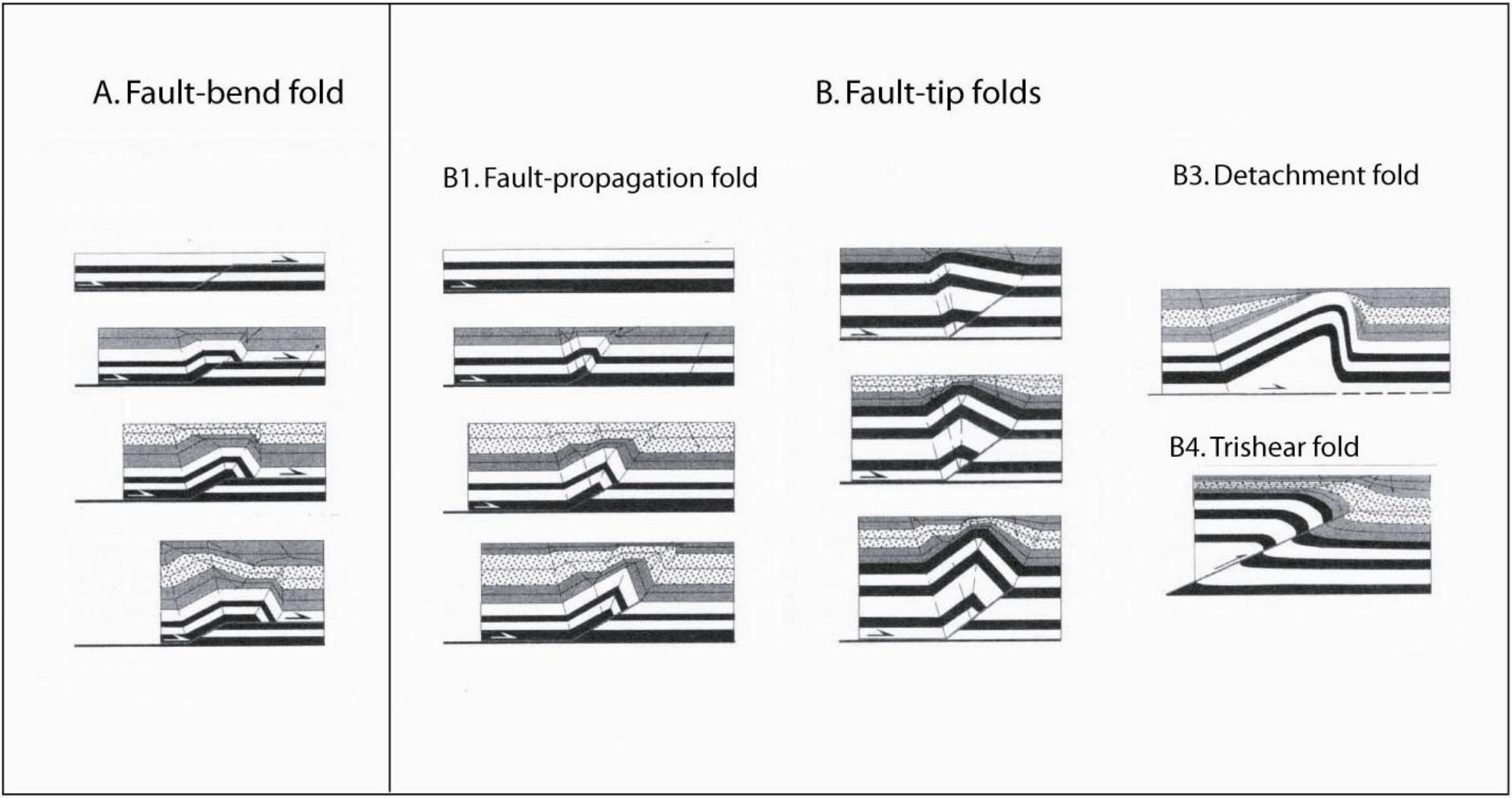
A. Fault-bend fold
B. Fault-tip folds
B1. Fault-propagation fold
B3. Detachment fold
B4. Trishear fold

figure 2

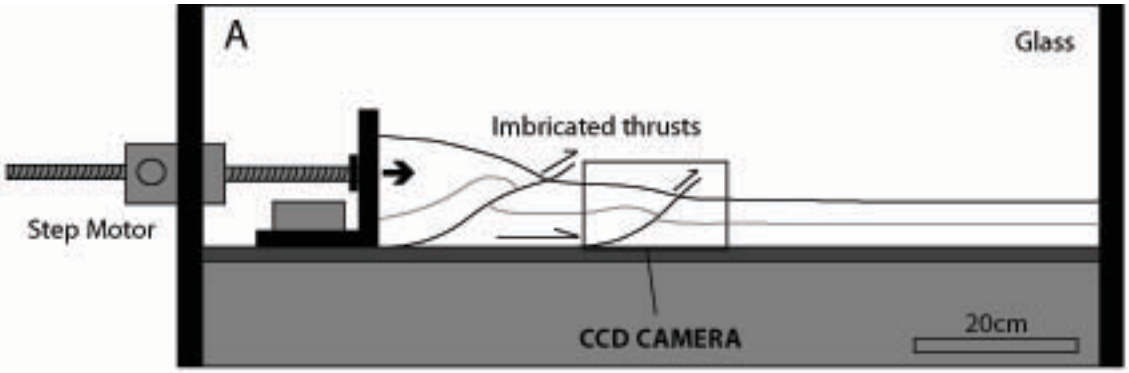

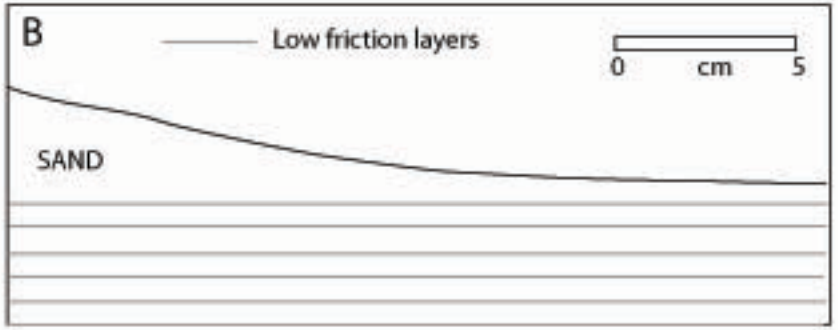

(C) CCD CAMERA IMAGES

IMAGE CORRELATION

DEFORMATION REPRESENTATION

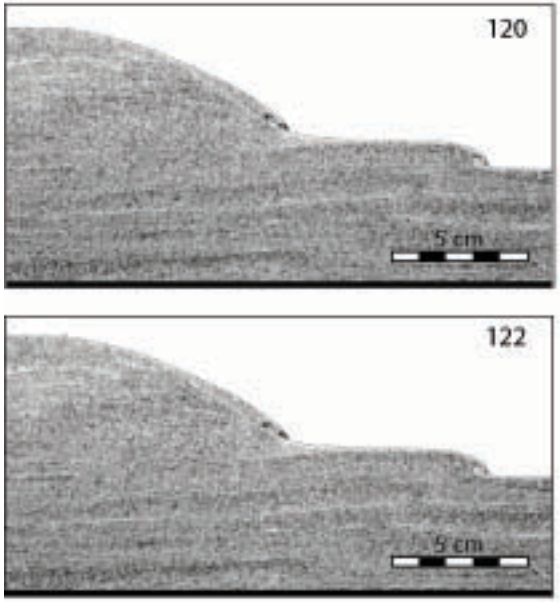

VIDEO PROCESSING

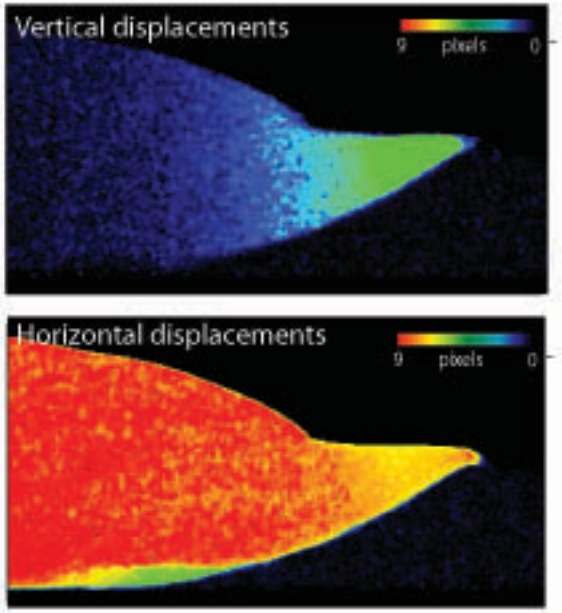

KINEMATIC ANALYSIS

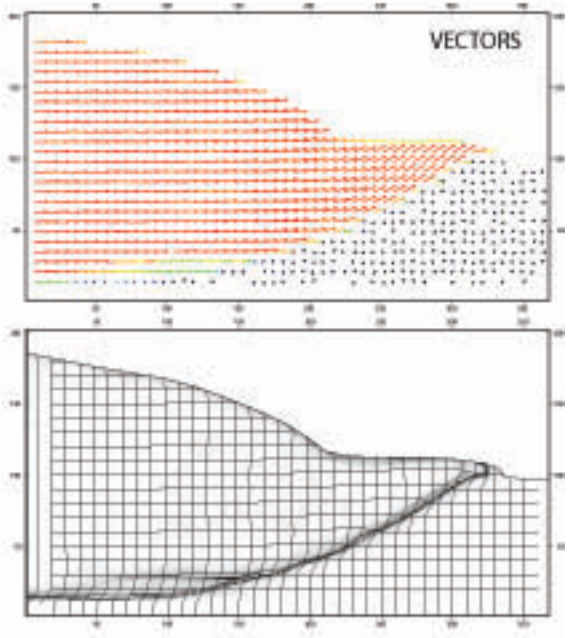

figure 3

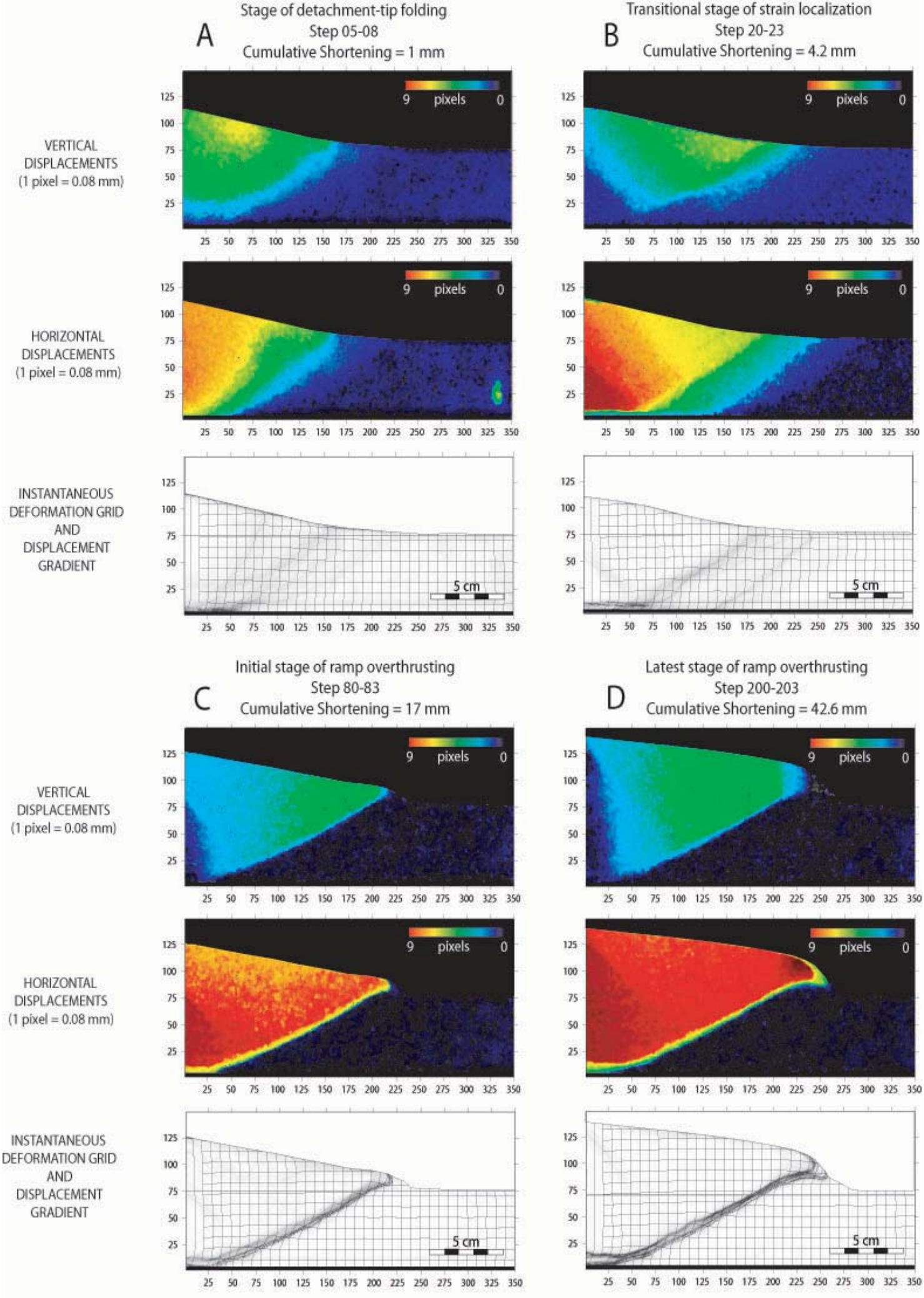
A
Stage of detachment-tip folding
Step 05-08
Cumulative Shortening = 1 mm
B
Transitional stage of strain localization
Step 20-23
Cumulative Shortening = 4.2 mm
C
Initial stage of ramp overthrusting
Step 80-83
Cumulative Shortening = 17 mm
D
Latest stage of ramp overthrusting
Step 200-203
Cumulative Shortening = 42.6 mm
VERTICAL DISPLACEMENTS (1 pixel = 0.08 mm)
HORIZONTAL DISPLACEMENTS (1 pixel = 0.08 mm)
INSTANTANEOUS DEFORMATION GRID AND DISPLACEMENT GRADIENT
9 pixels 0
5 cm

figure 4

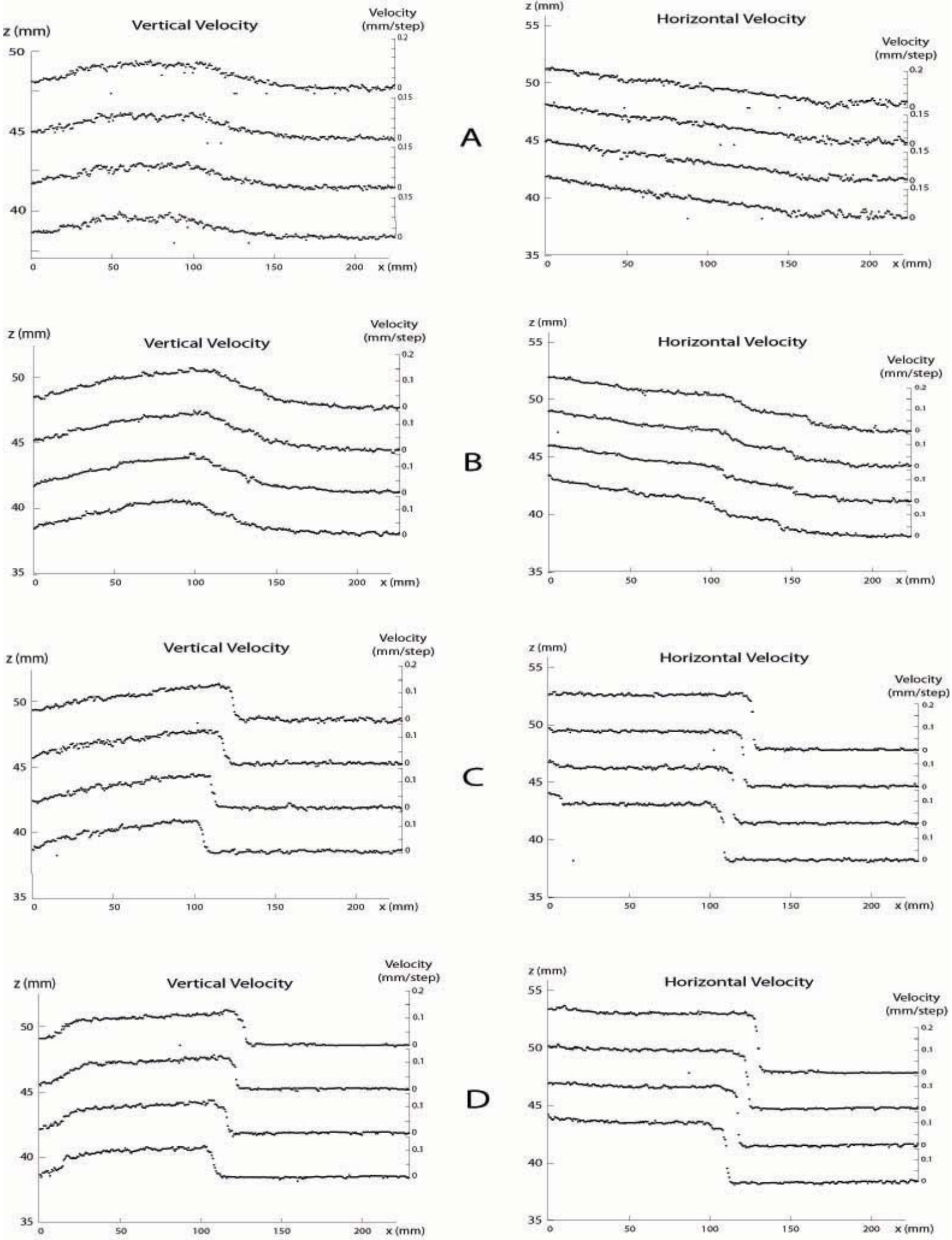
Vertical Velocity
Horizontal Velocity
z (mm)
x (mm)
Velocity (mm/step)
A
B
C
D

figure 5

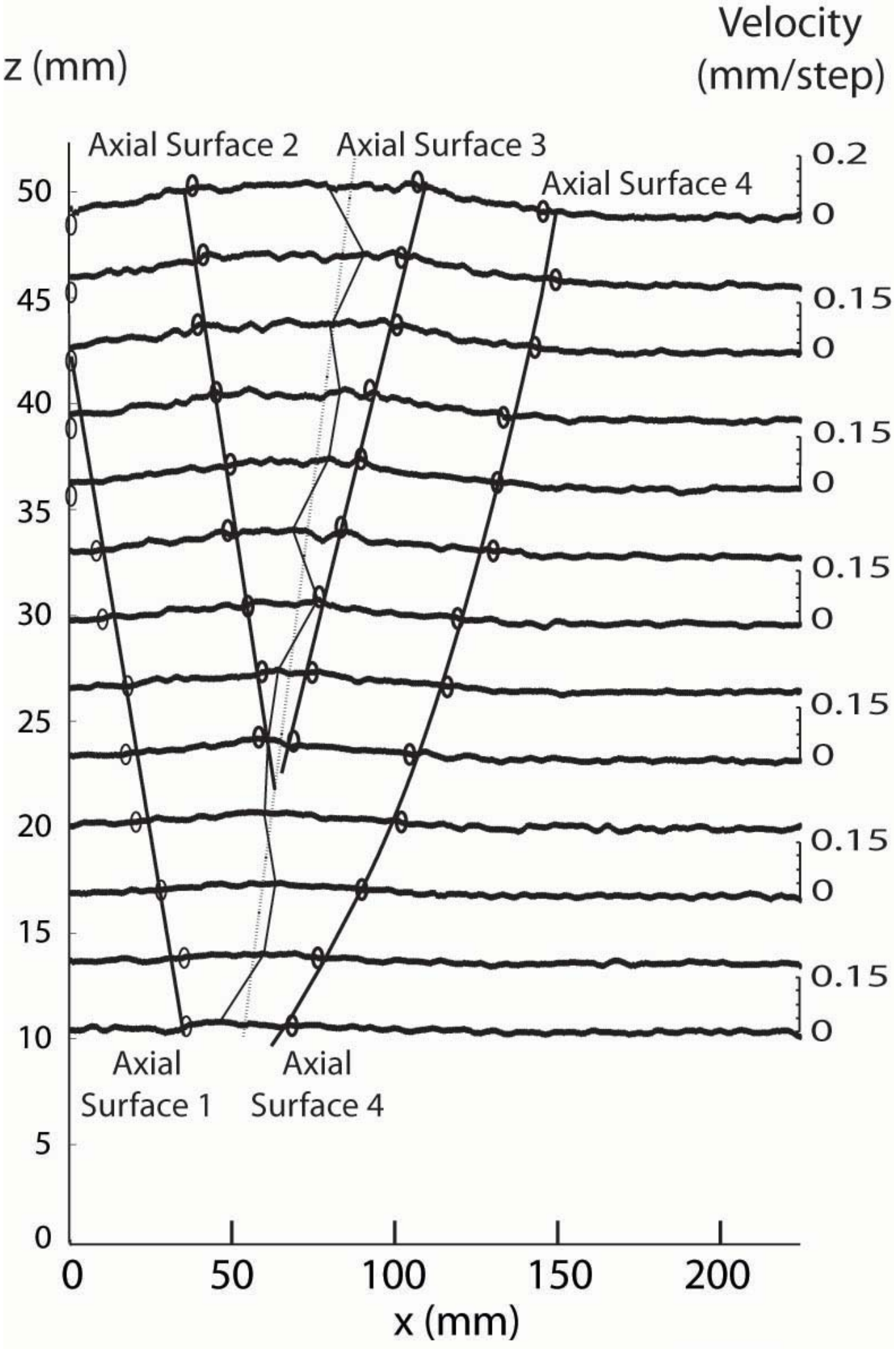
z (mm)
Velocity
(mm/step)
Axial Surface 2
Axial Surface 3
Axial Surface 4
Axial
Surface 1
Axial
Surface 4
50
45
40
35
30
25
20
15
10
5
0
0
50
100
150
200
x (mm)
0.2
0
0.15
0
0.15
0
0.15
0
0.15
0
0.15
0
0.15
0

figure 6

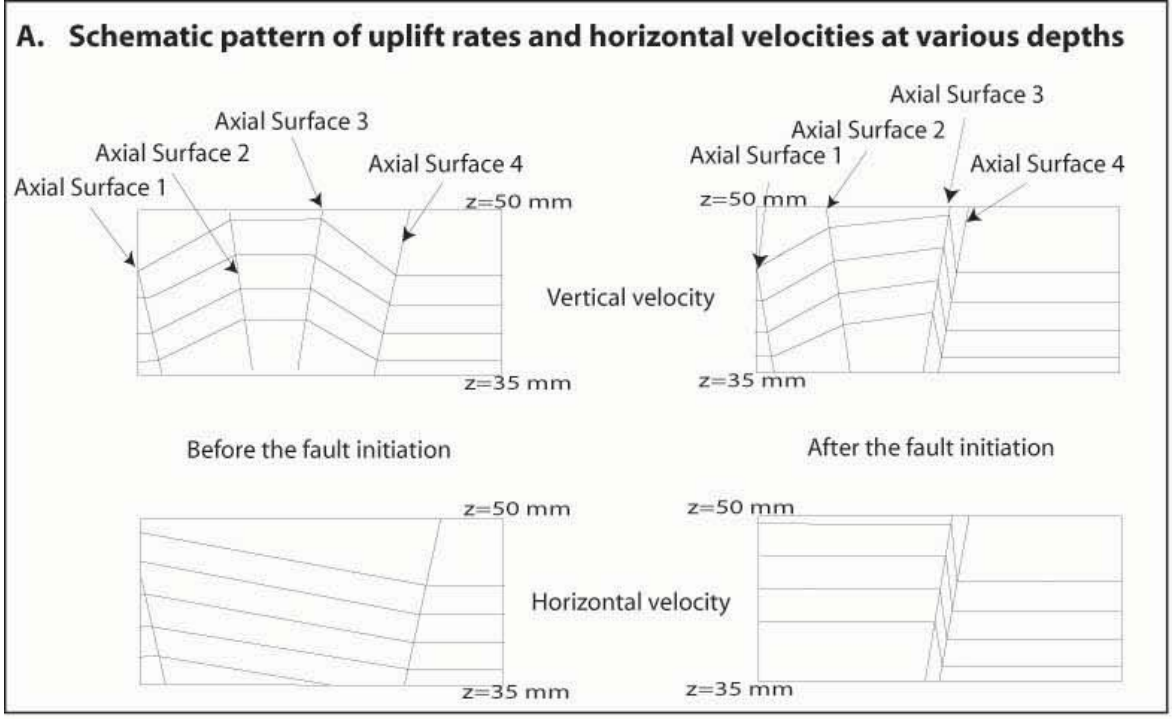
A. Schematic pattern of uplift rates and horizontal velocities at various depths
Axial Surface 1
Axial Surface 2
Axial Surface 3
Axial Surface 4
z=50 mm
z=35 mm
Vertical velocity
Before the fault initiation
After the fault initiation
Horizontal velocity

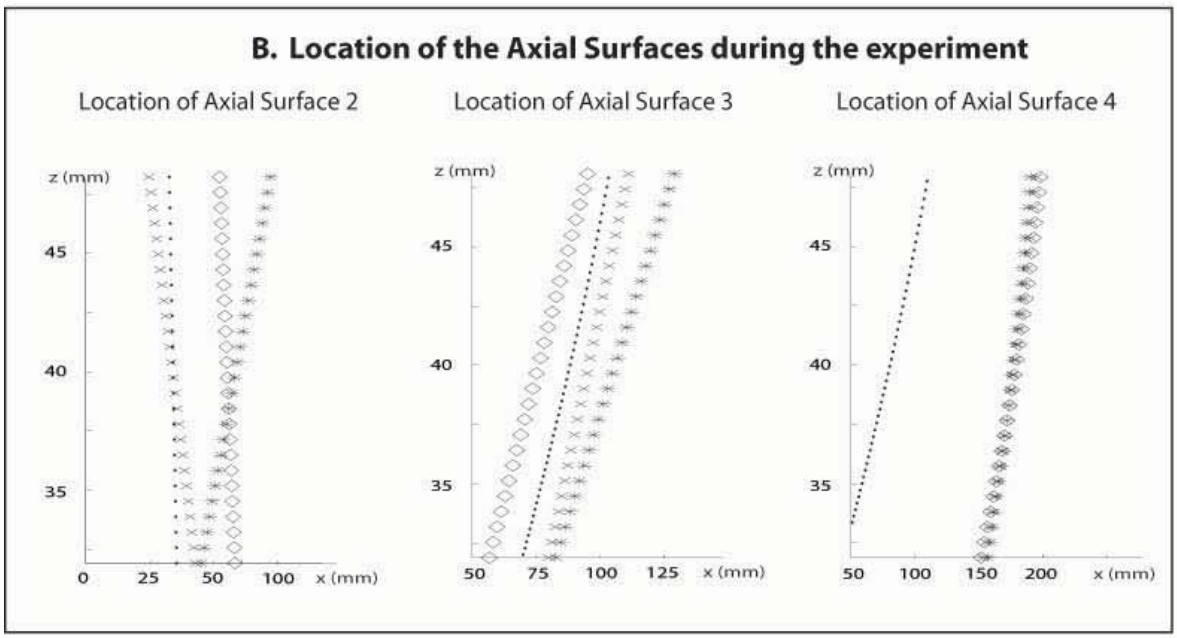
B. Location of the Axial Surfaces during the experiment
Location of Axial Surface 2
Location of Axial Surface 3
Location of Axial Surface 4
z (mm)
x (mm)

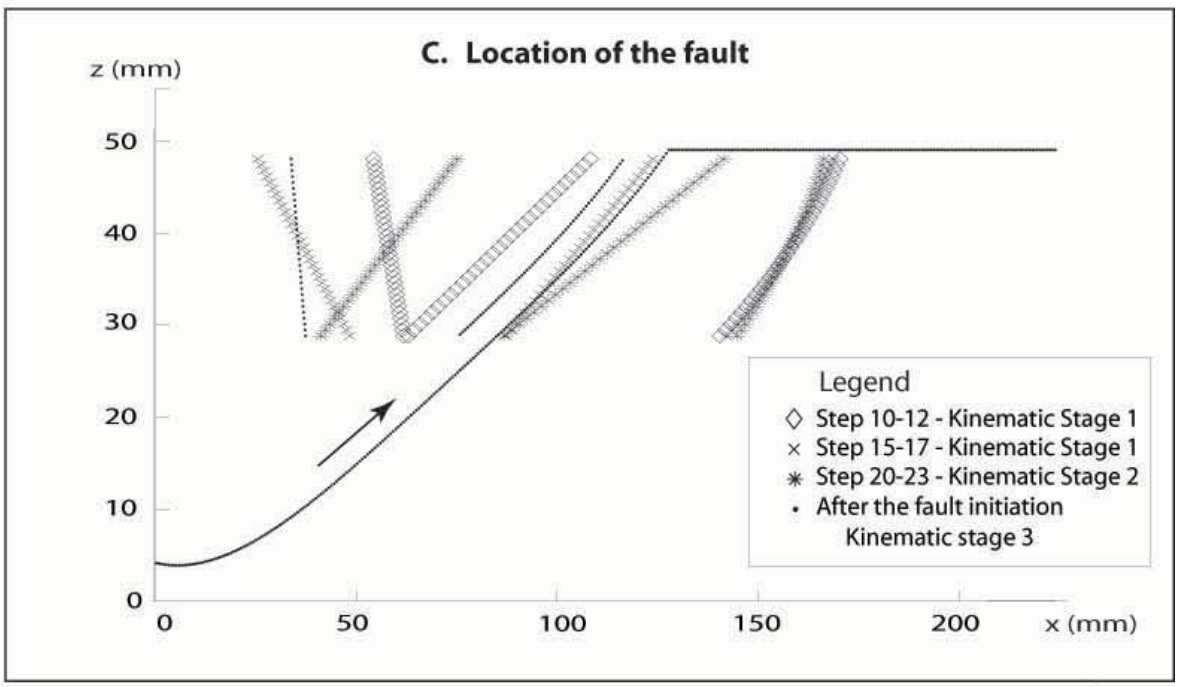
C. Location of the fault
z (mm)
x (mm)
Legend
Step 10-12 - Kinematic Stage 1
Step 15-17 - Kinematic Stage 1
Step 20-23 - Kinematic Stage 2
After the fault initiation
Kinematic stage 3

figure 7

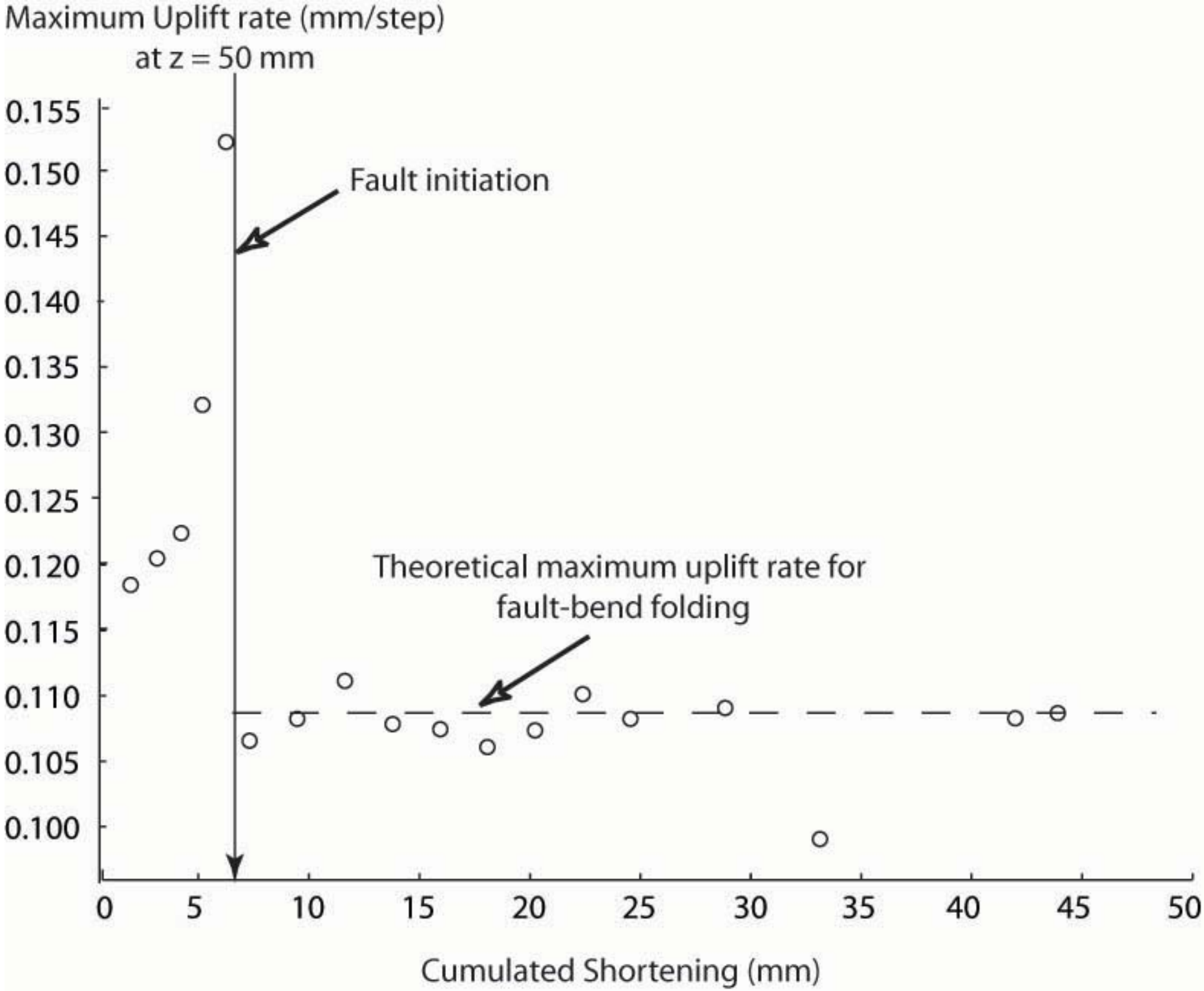
Maximum Uplift rate (mm/step)
at z = 50 mm
0.155
0.150
0.145
0.140
0.135
0.130
0.125
0.120
0.115
0.110
0.105
0.100
Fault initiation
Theoretical maximum uplift rate for
fault-bend folding
0
5
10
15
20
25
30
35
40
45
50
Cumulated Shortening (mm)

figure 8

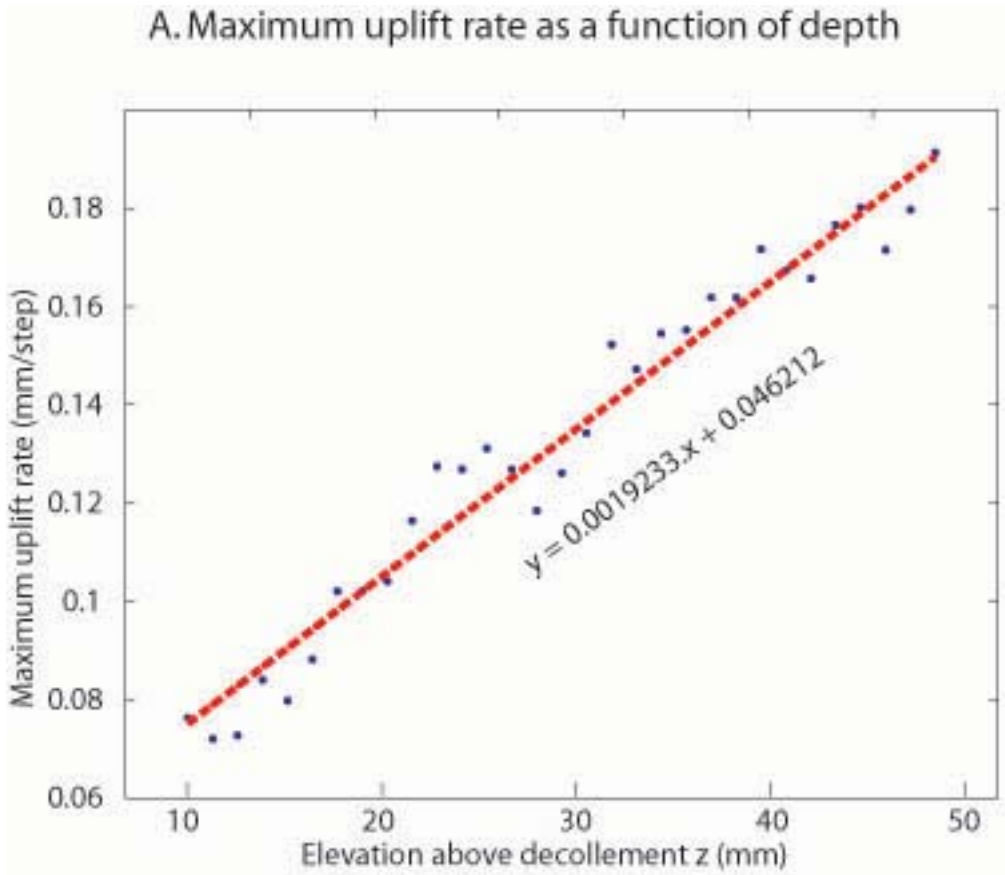
A. Maximum uplift rate as a function of depth
Maximum uplift rate (mm/step)
0.18
0.16
0.14
0.12
0.1
0.08
0.06
10
20
30
40
50
Elevation above decollement z (mm)
y = 0.0019233.x + 0.046212

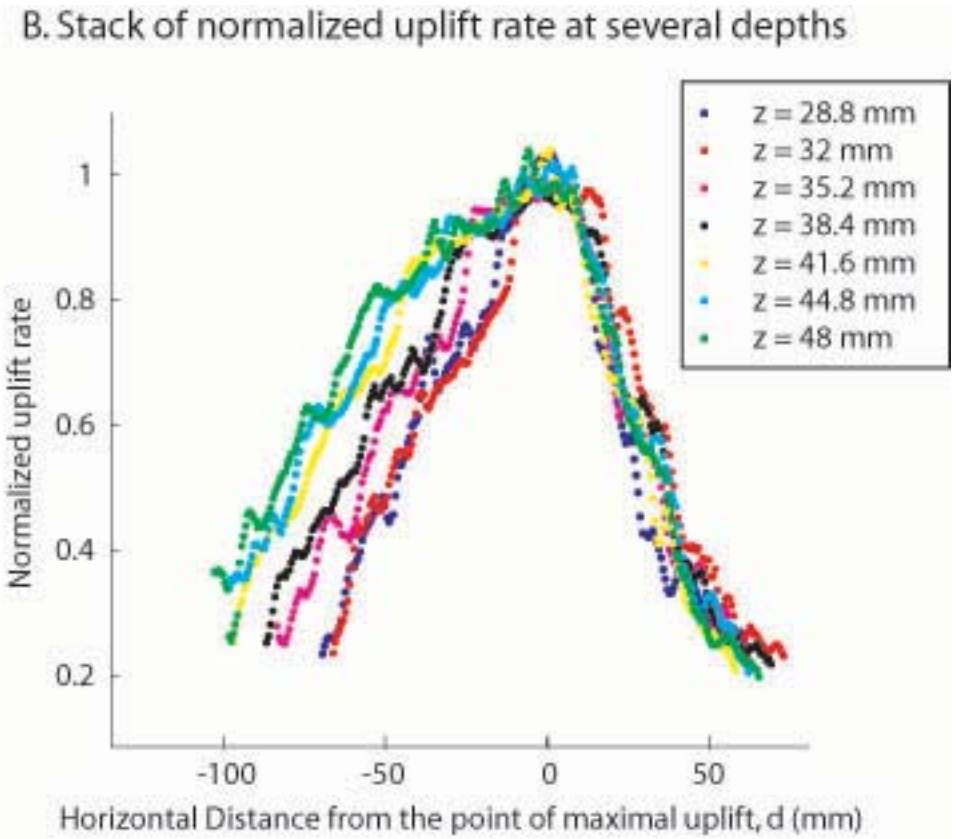
B. Stack of normalized uplift rate at several depths
Normalized uplift rate
1
0.8
0.6
0.4
0.2
-100
-50
0
50
Horizontal Distance from the point of maximal uplift, d (mm)
z = 28.8 mm
z = 32 mm
z = 35.2 mm
z = 38.4 mm
z = 41.6 mm
z = 44.8 mm
z = 48 mm

figure 9

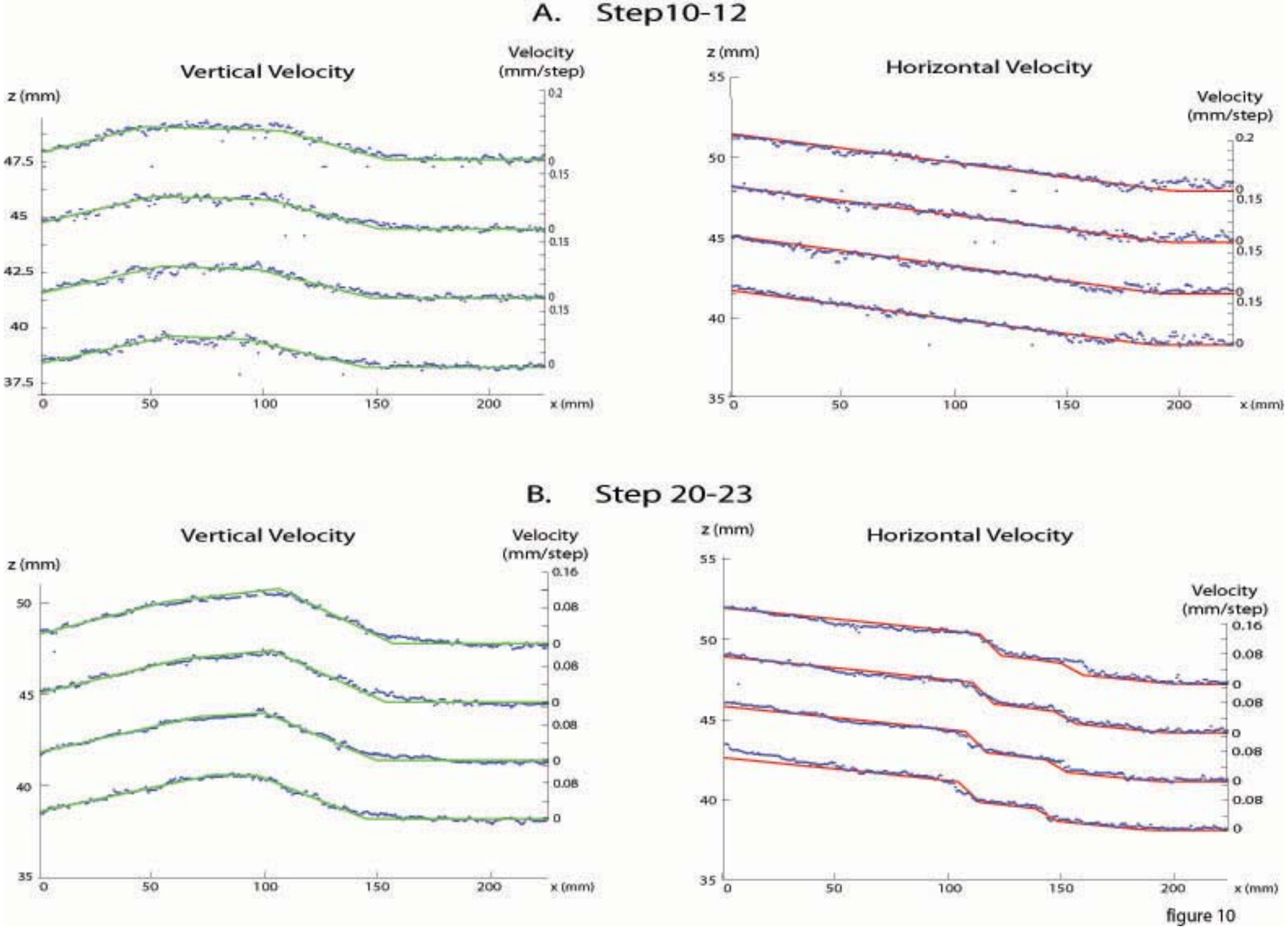
A. Step10-12
Vertical Velocity
Velocity (mm/step)
z (mm)
47.5
45
42.5
40
37.5
0.2
0.15
0
0
0.15
0
0.15
0
0
50
100
150
200
x (mm)
Horizontal Velocity
z (mm)
55
50
45
40
35
Velocity (mm/step)
0.2
0.15
0
0.15
0
0.15
0
0
50
100
150
200
x (mm)
B. Step 20-23
Vertical Velocity
Velocity (mm/step)
z (mm)
50
45
40
35
0.16
0.08
0
0.08
0
0.08
0
0.08
0
0
50
100
150
200
x (mm)
Horizontal Velocity
z (mm)
55
50
45
40
35
Velocity (mm/step)
0.16
0.08
0
0.08
0
0.08
0
0.08
0
0
50
100
150
200
x (mm)

figure 10

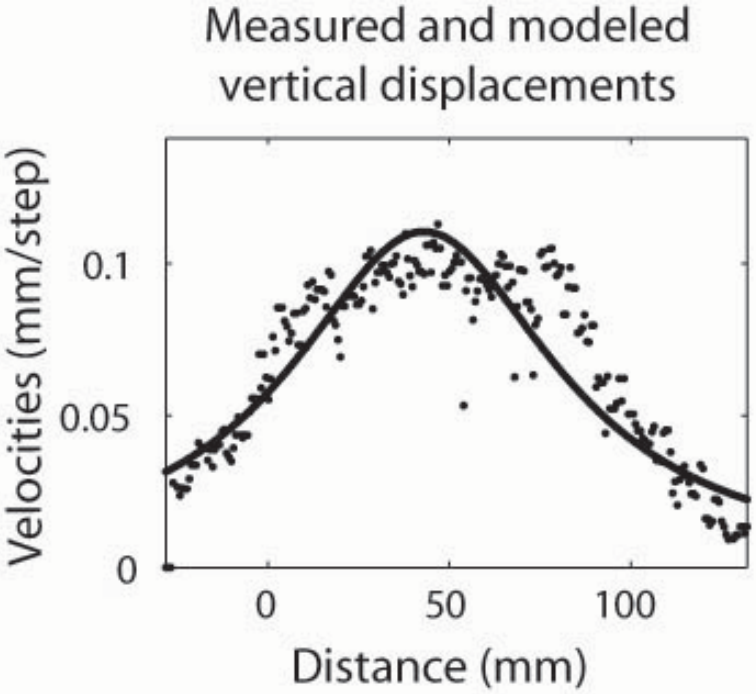
Measured and modeled
vertical displacements
Velocities (mm/step)
0.1
0.05
0
0
50
100
Distance (mm)

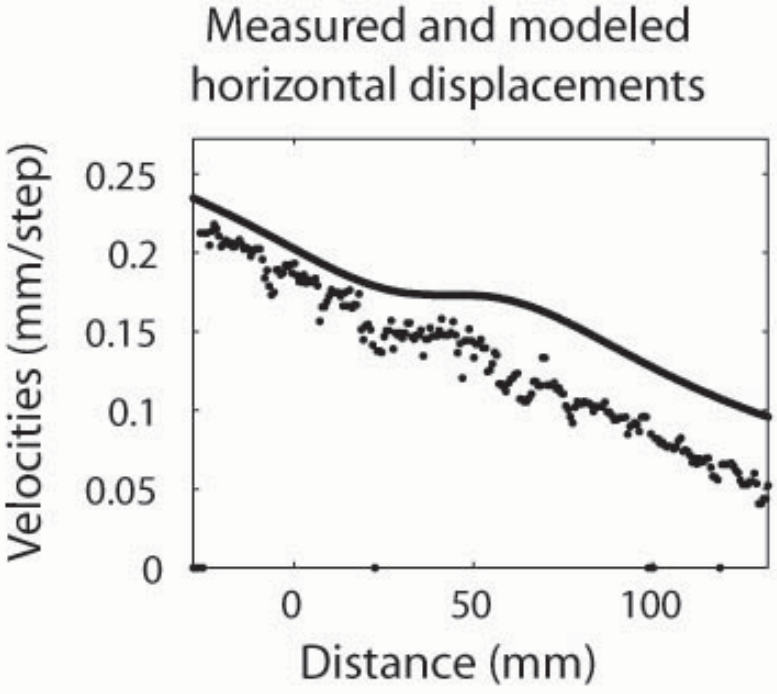
Measured and modeled
horizontal displacements
Velocities (mm/step)
0.25
0.2
0.15
0.1
0.05
0
0
50
100
Distance (mm)

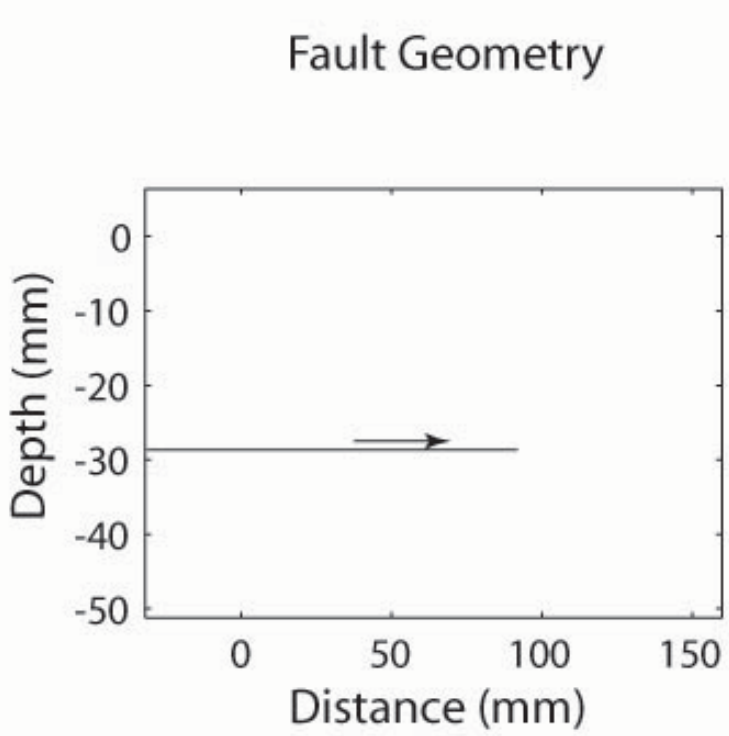
Fault Geometry
Depth (mm)
0
-10
-20
-30
-40
-50
0
50
100
150
Distance (mm)

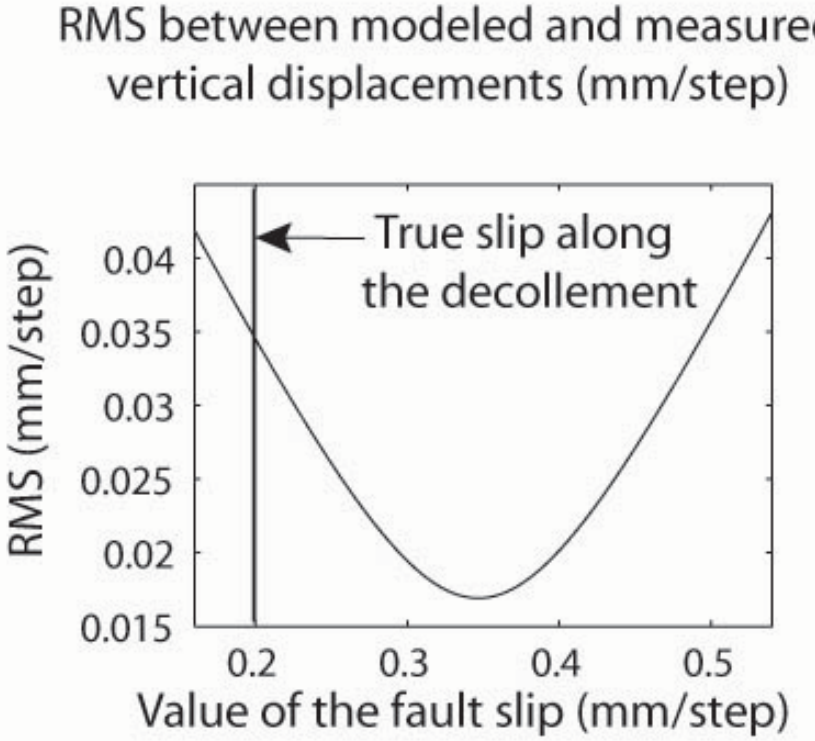
RMS between modeled and measured
vertical displacements (mm/step)
RMS (mm/step)
0.04
0.035
0.03
0.025
0.02
0.015
True slip along
the decollement
0.2
0.3
0.4
0.5
Value of the fault slip (mm/step)

figure 11

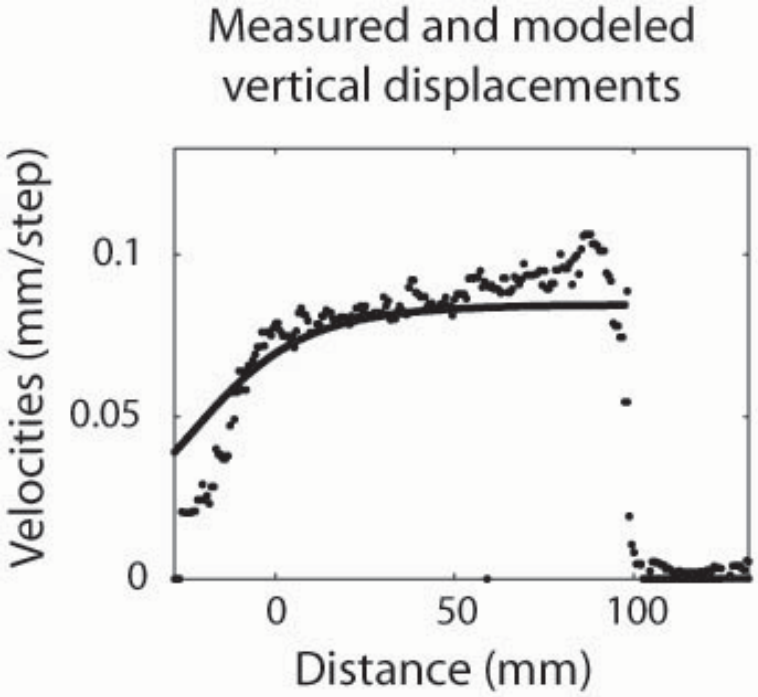
Measured and modeled
vertical displacements
Velocities (mm/step)
0.1
0.05
0
0
50
100
Distance (mm)

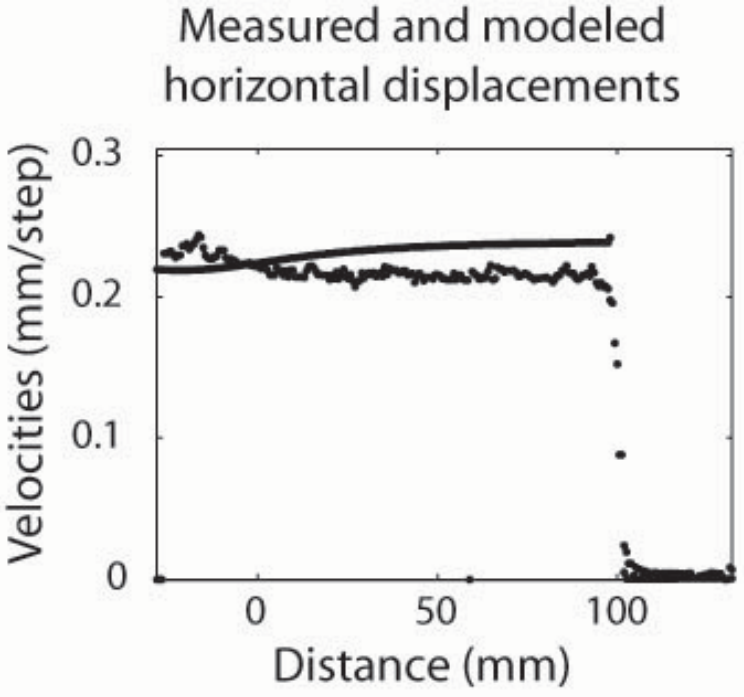
Measured and modeled
horizontal displacements
Velocities (mm/step)
0.3
0.2
0.1
0
0
50
100
Distance (mm)

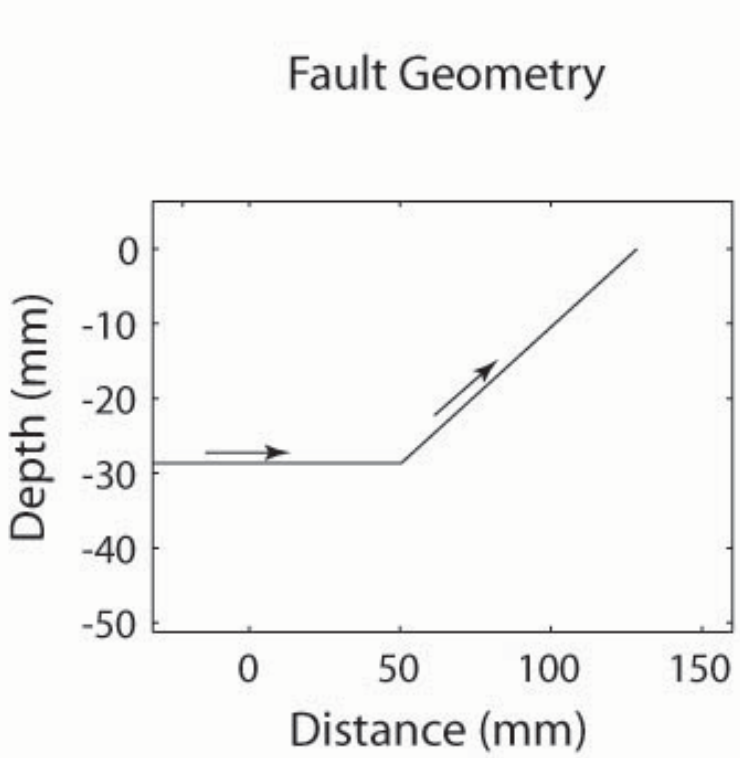
Fault Geometry
Depth (mm)
0
-10
-20
-30
-40
-50
0
50
100
150
Distance (mm)

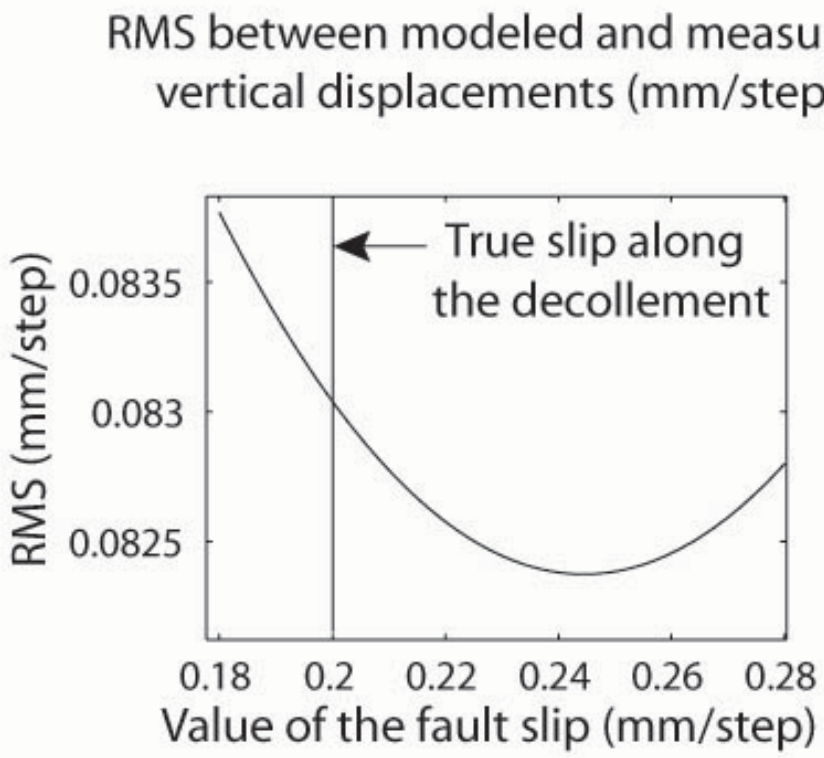
RMS between modeled and measured
vertical displacements (mm/step)
RMS (mm/step)
0.0835
0.083
0.0825
True slip along
the decollement
0.18
0.2
0.22
0.24
0.26
0.28
Value of the fault slip (mm/step)

figure 12

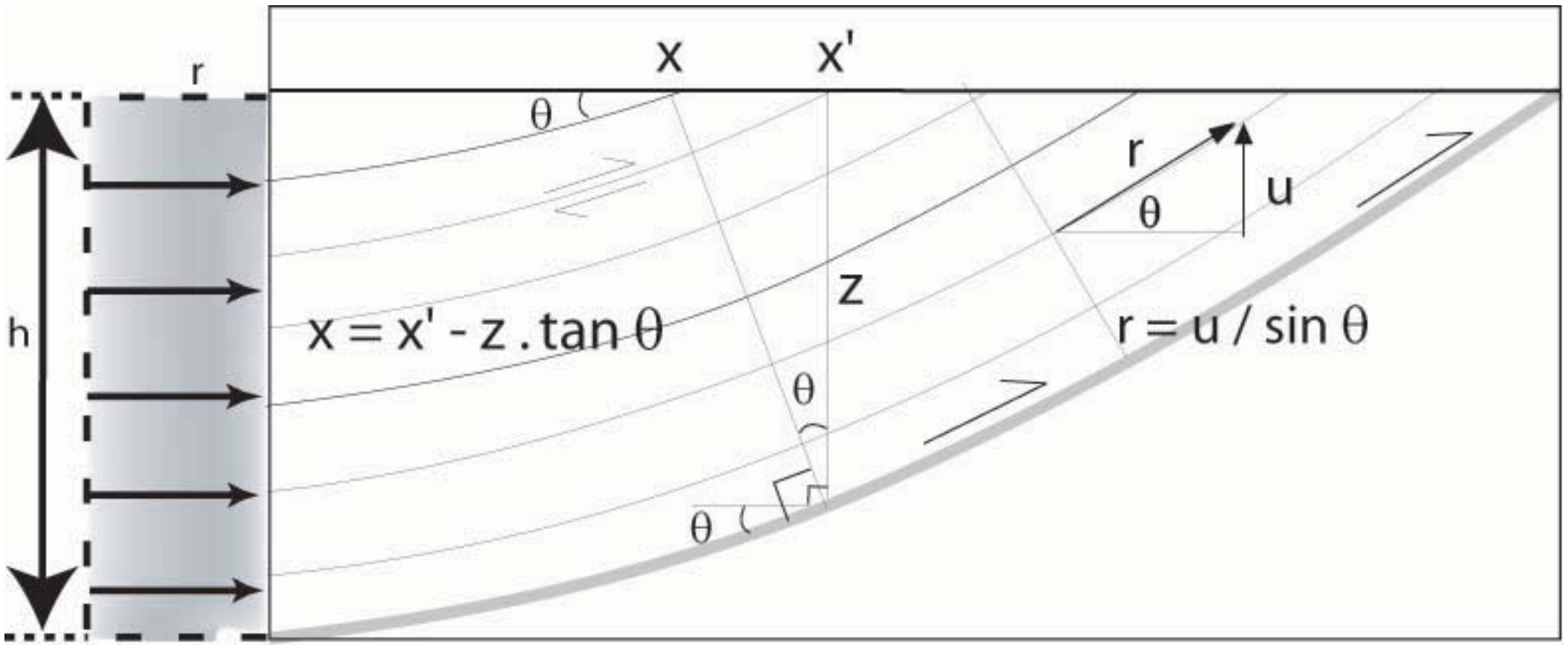

figure 13

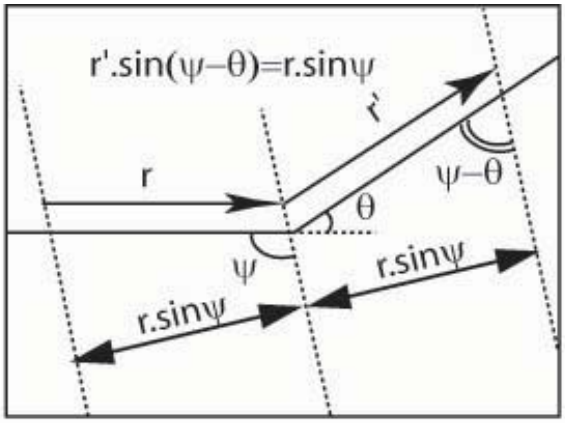

$$r' = \frac{r.\sin\psi}{\sin(\psi-\theta)}$$

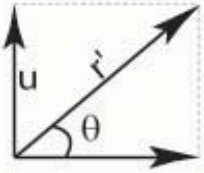

$r' \sim u/\sin\theta$

$$r = \frac{u.\sin(\psi-\theta)}{\sin\psi.\sin\theta}$$

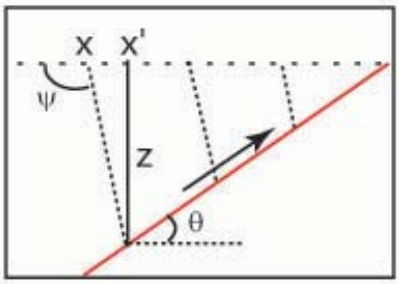

$x = x' + z/\tan\psi$

Finite deformation of a level initially horizontal (dashed line)

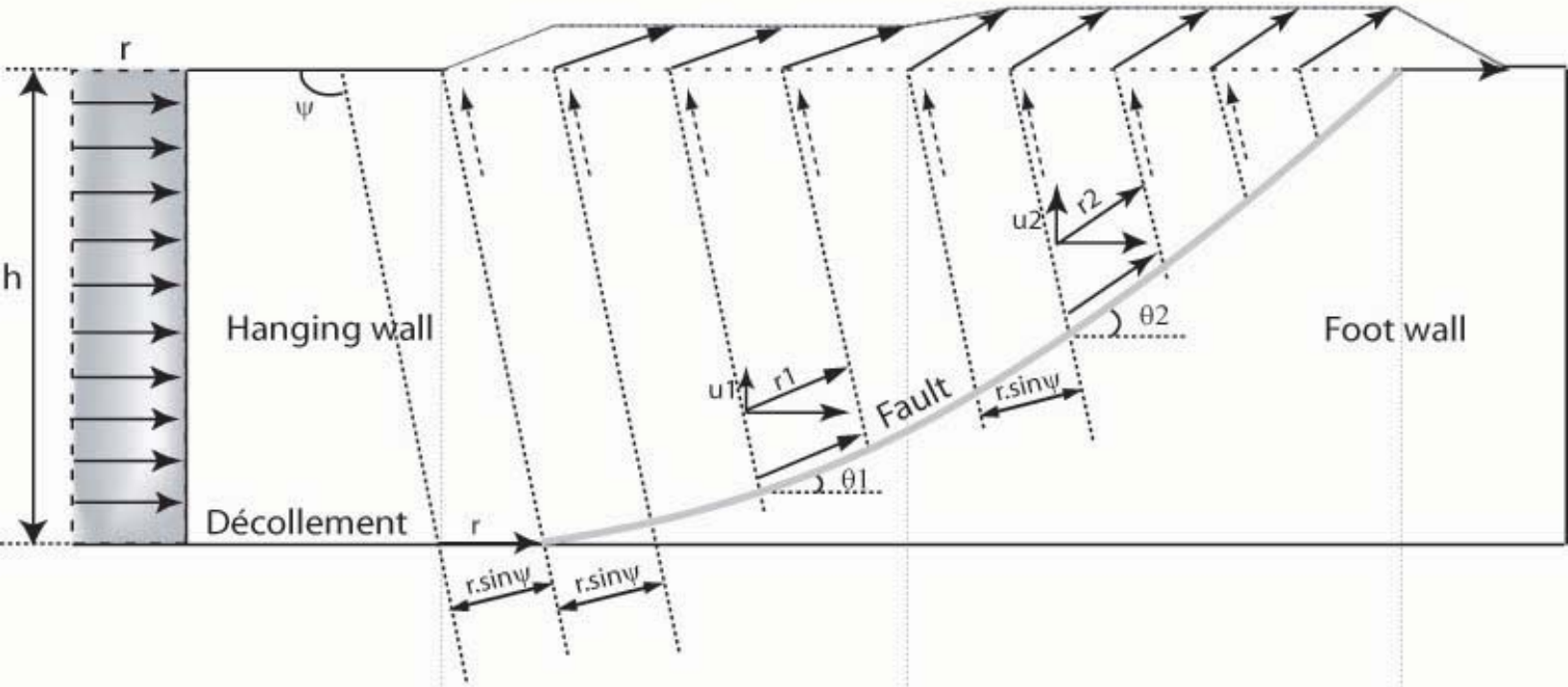

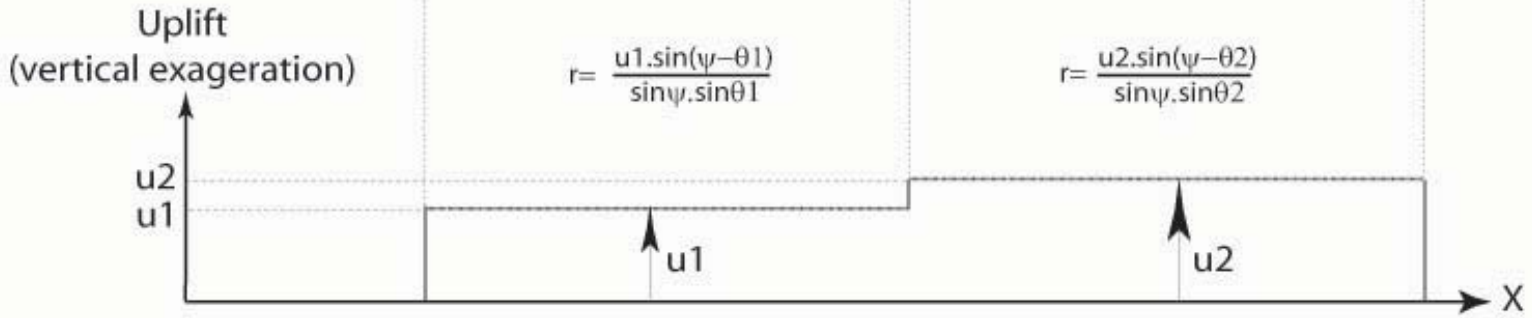

$$r = \frac{u1.\sin(\psi-\theta1)}{\sin\psi.\sin\theta1}$$

$$r = \frac{u2.\sin(\psi-\theta2)}{\sin\psi.\sin\theta2}$$

Uplift du to an increment of shortening
(equivalent to the instantaneous vertical velocity)

figure 14

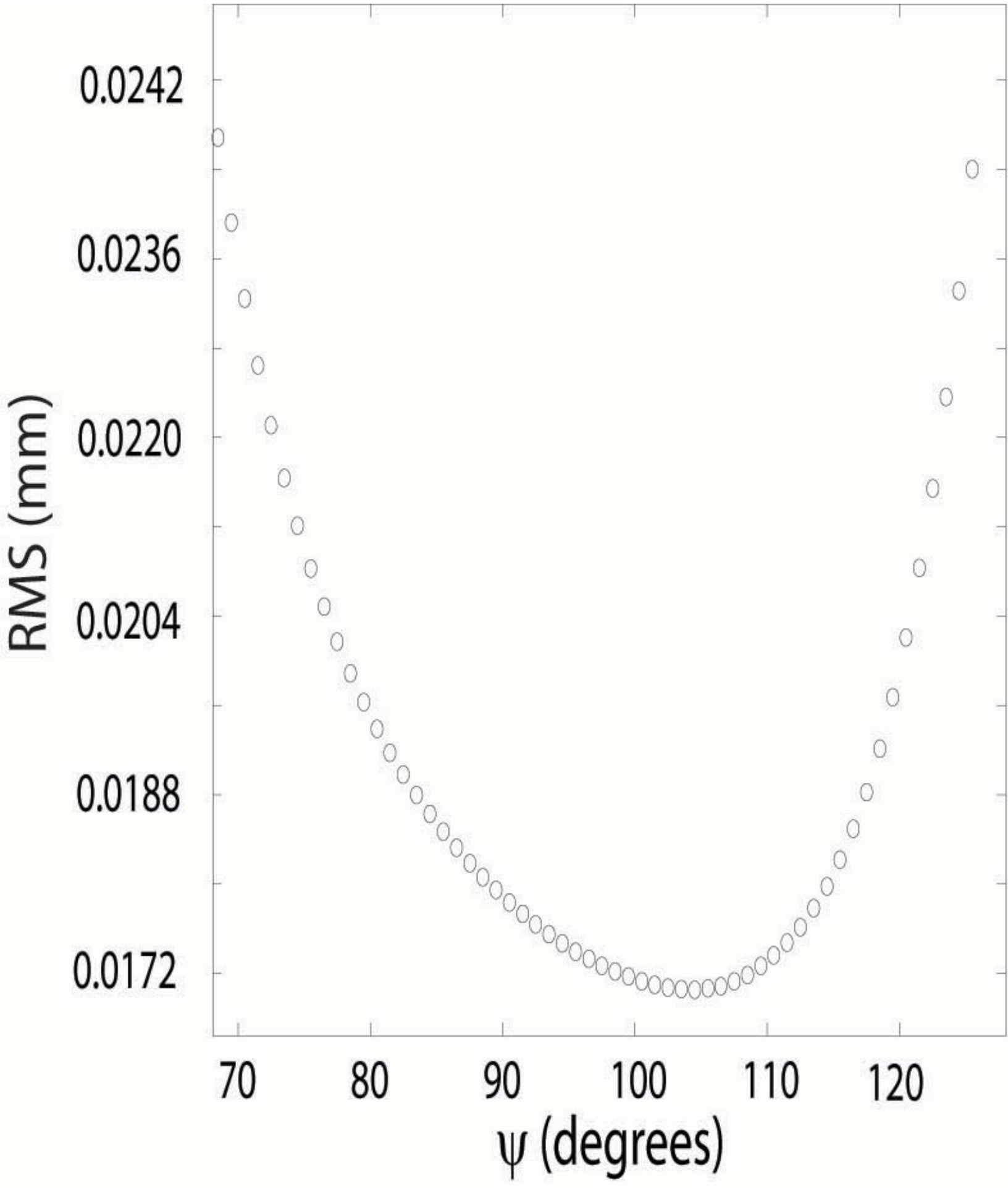
0.0242
0.0236
0.0220
0.0204
0.0188
0.0172
RMS (mm)
70
80
90
100
110
120
ψ (degrees)

figure 15

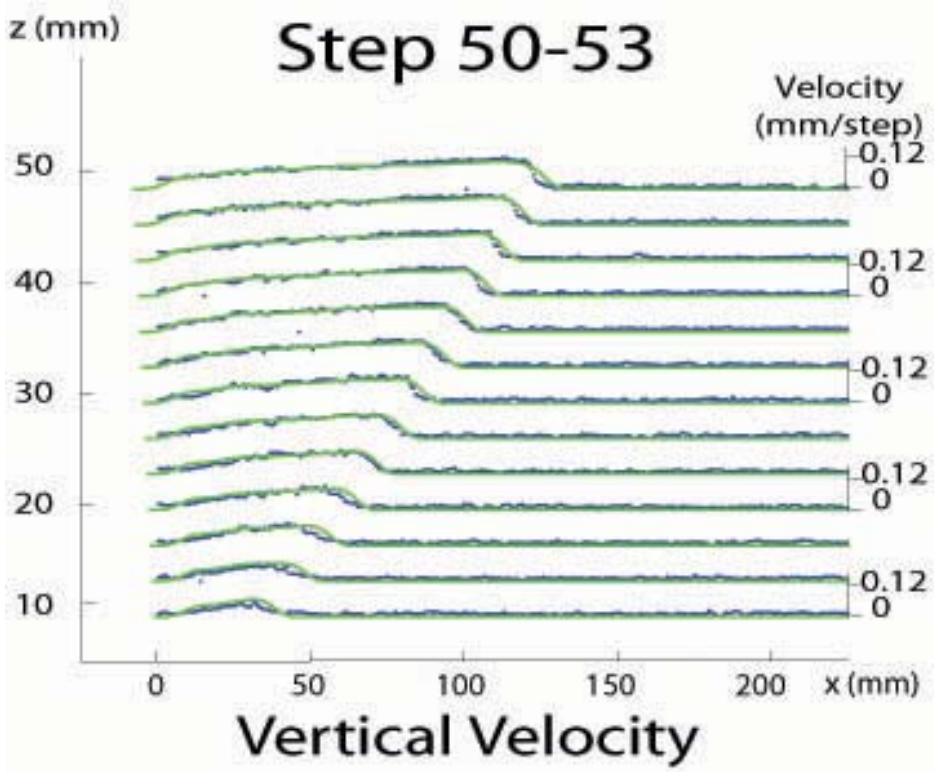
Step 50-53
z (mm)
Velocity
(mm/step)
0.12
0
50
40
30
20
10
0
50
100
150
200
x (mm)
Vertical Velocity

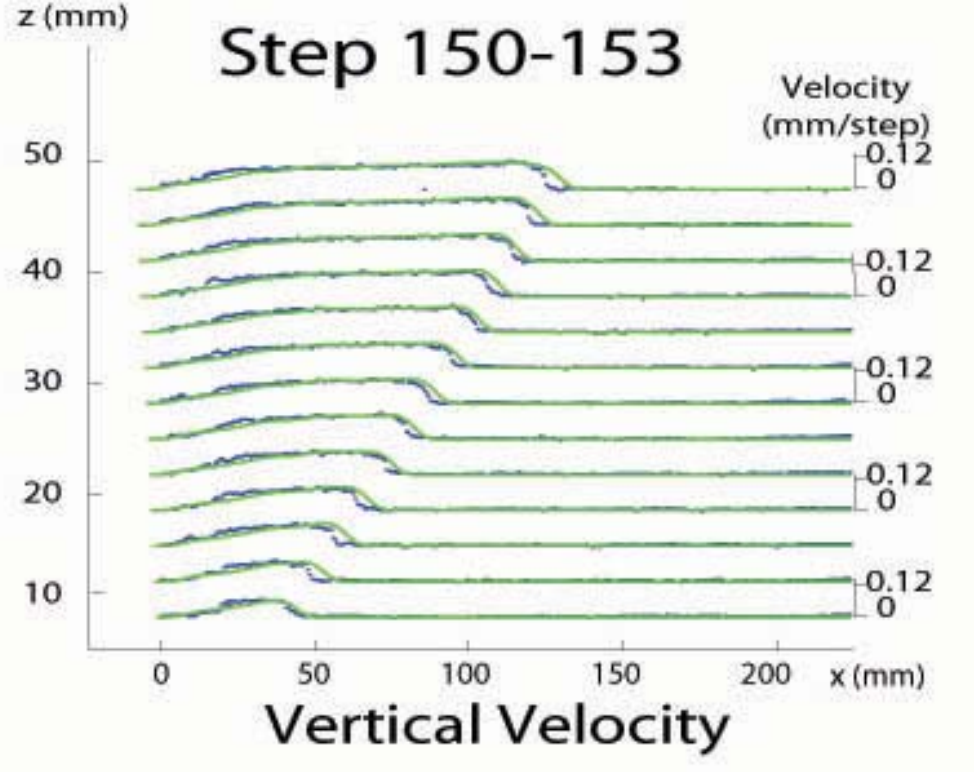
Step 150-153
z (mm)
Velocity
(mm/step)
0.12
0
50
40
30
20
10
0
50
100
150
200
x (mm)
Vertical Velocity

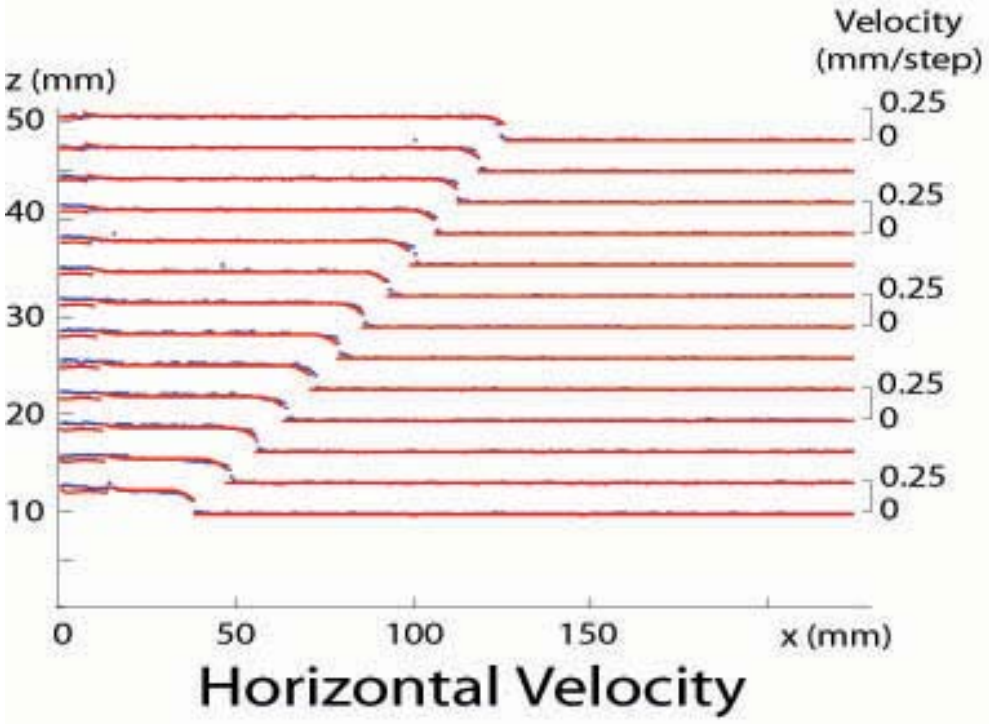
Velocity
(mm/step)
z (mm)
0.25
0
50
40
30
20
10
0
50
100
150
x (mm)
Horizontal Velocity

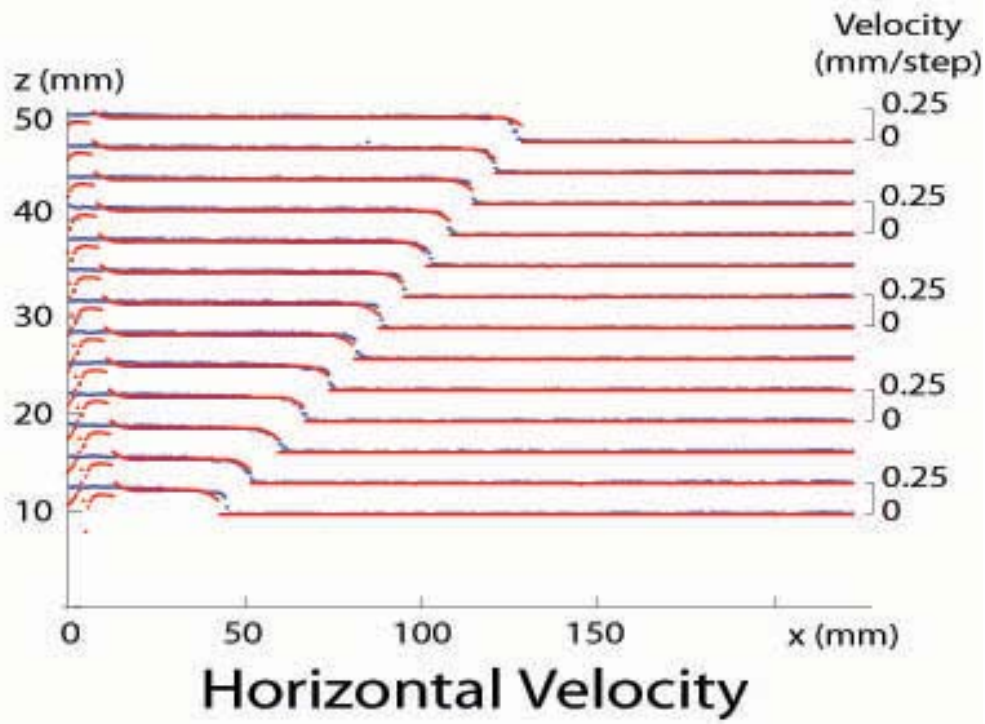
Velocity
(mm/step)
z (mm)
0.25
0
50
40
30
20
10
0
50
100
150
x (mm)
Horizontal Velocity

figure 16

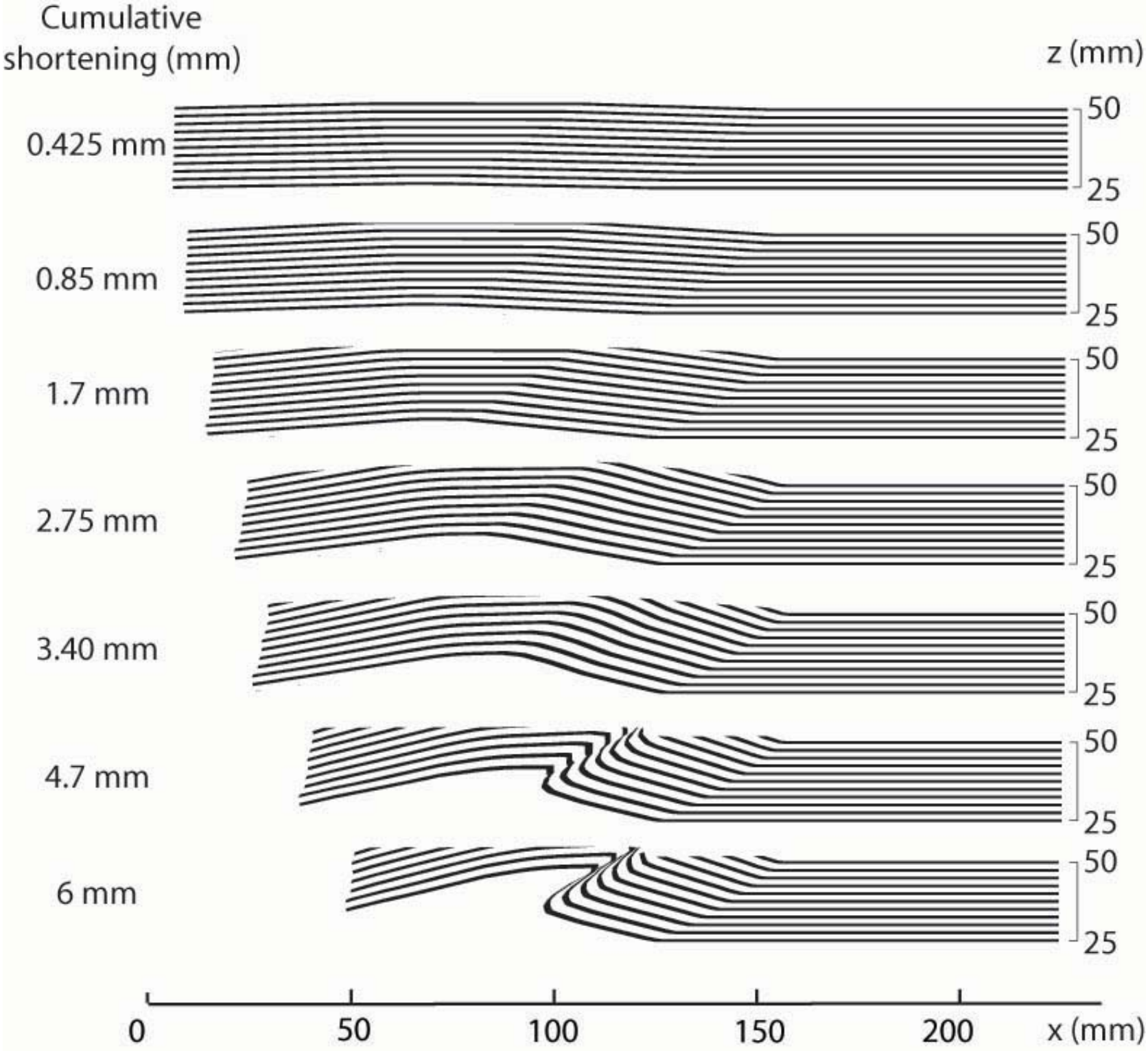
Cumulative shortening (mm)
z (mm)
0.425 mm
0.85 mm
1.7 mm
2.75 mm
3.40 mm
4.7 mm
6 mm
50
25
0
50
100
150
200
x (mm)

figure 17

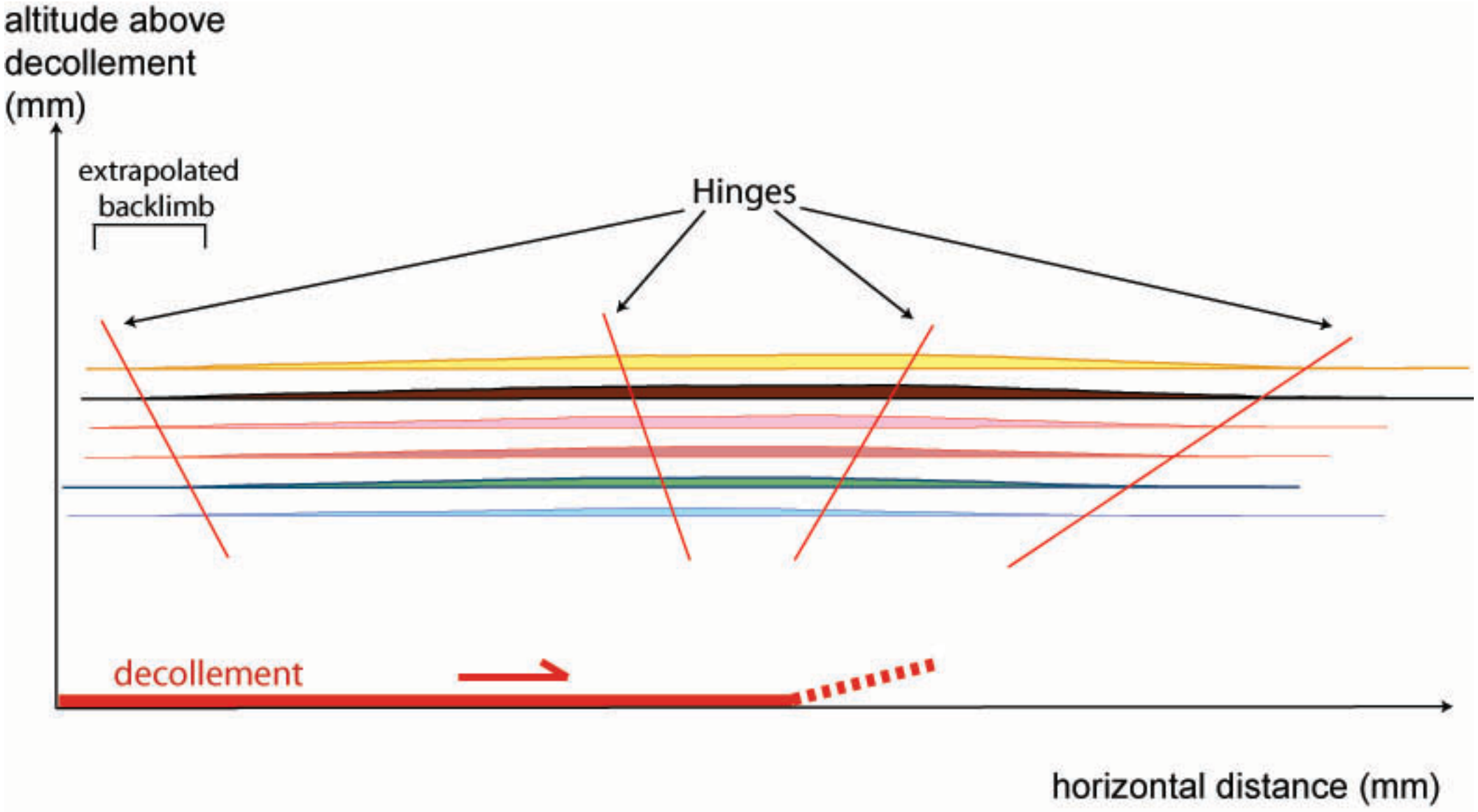
altitude above
decollement
(mm)
extrapolated
backlimb
Hinges
decollement
horizontal distance (mm)

figure 18

A

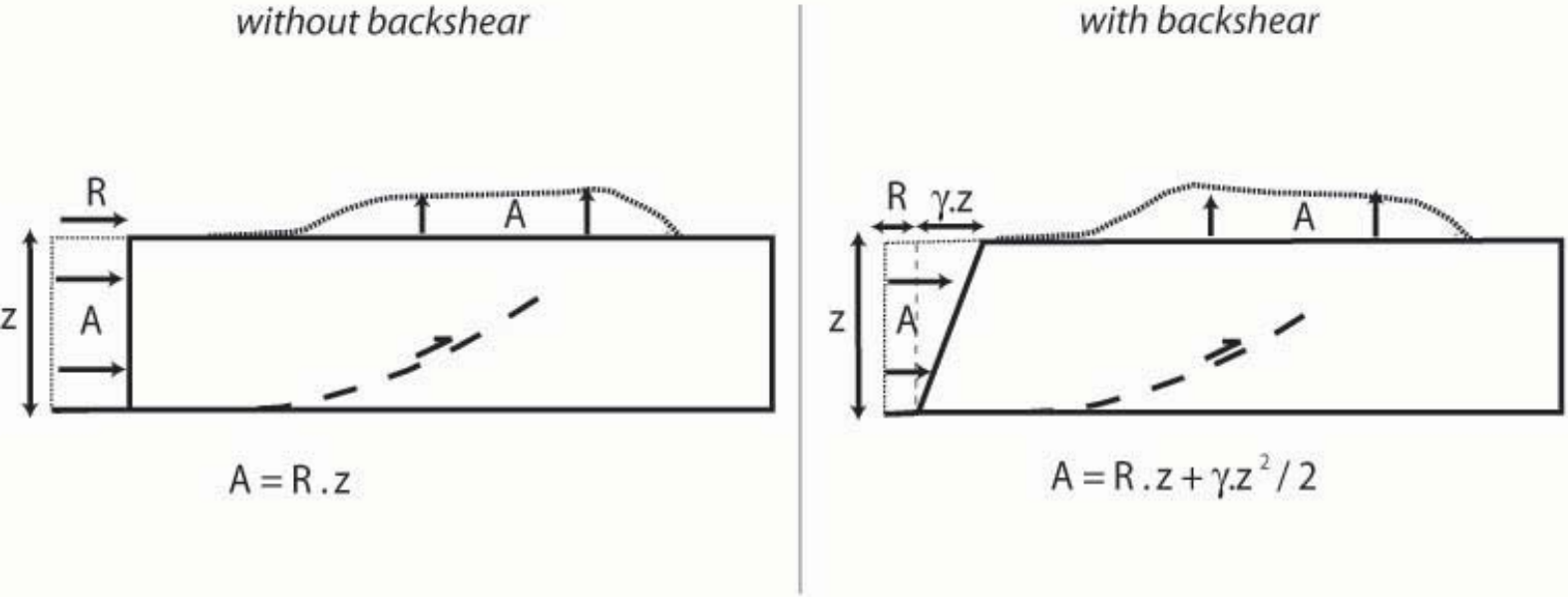
without backshear
with backshear
R
A
z
A
R
γ.z
A
z
A
A = R . z
A = R . z + γ.z² / 2

B

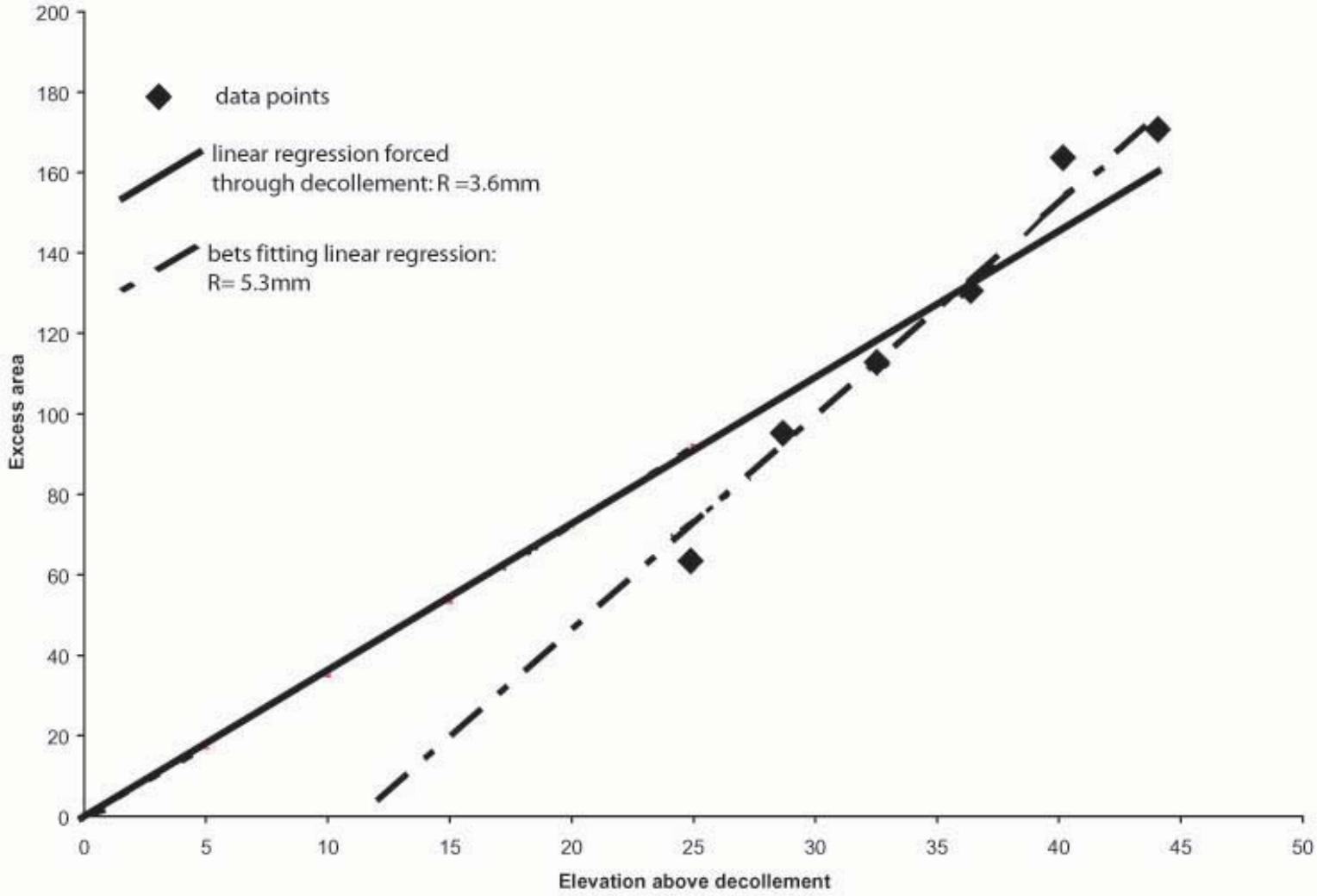
data points
linear regression forced through decollement: R =3.6mm
bets fitting linear regression: R= 5.3mm
Excess area
Elevation above decollement
0
20
40
60
80
100
120
140
160
180
200
0
5
10
15
20
25
30
35
40
45
50

figure 19

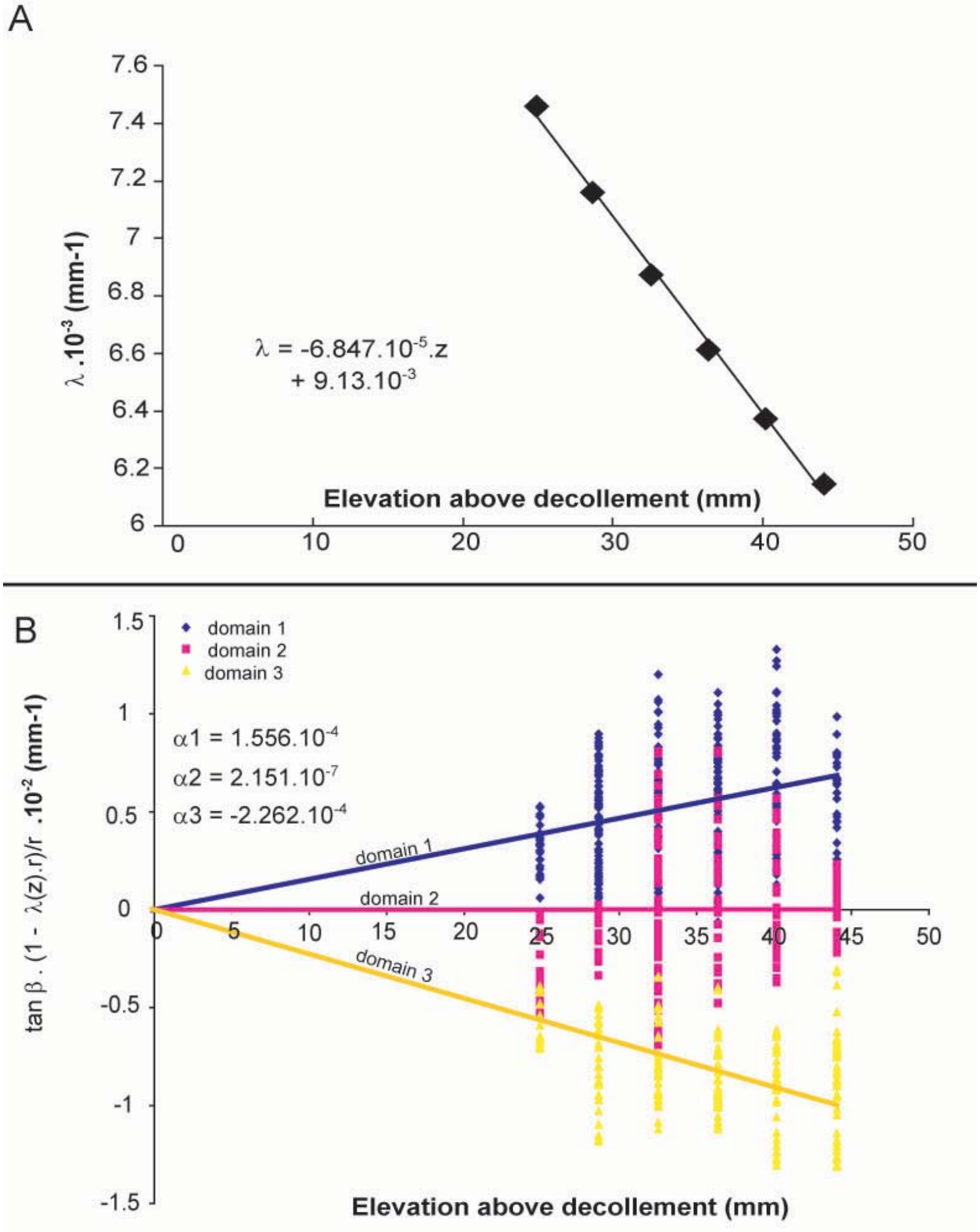
A
7.6
7.4
7.2
7
6.8
6.6
6.4
6.2
6
λ .10-3 (mm-1)
λ = -6.847.10-5.z
+ 9.13.10-3
Elevation above decollement (mm)
0
10
20
30
40
50
B
1.5
1
0.5
0
-0.5
-1
-1.5
domain 1
domain 2
domain 3
α1 = 1.556.10-4
α2 = 2.151.10-7
α3 = -2.262.10-4
tan β . (1 - λ(z).r)/r .10-2 (mm-1)
domain 1
domain 2
domain 3
0
5
10
15
20
25
30
35
40
45
50
Elevation above decollement (mm)

figure 20

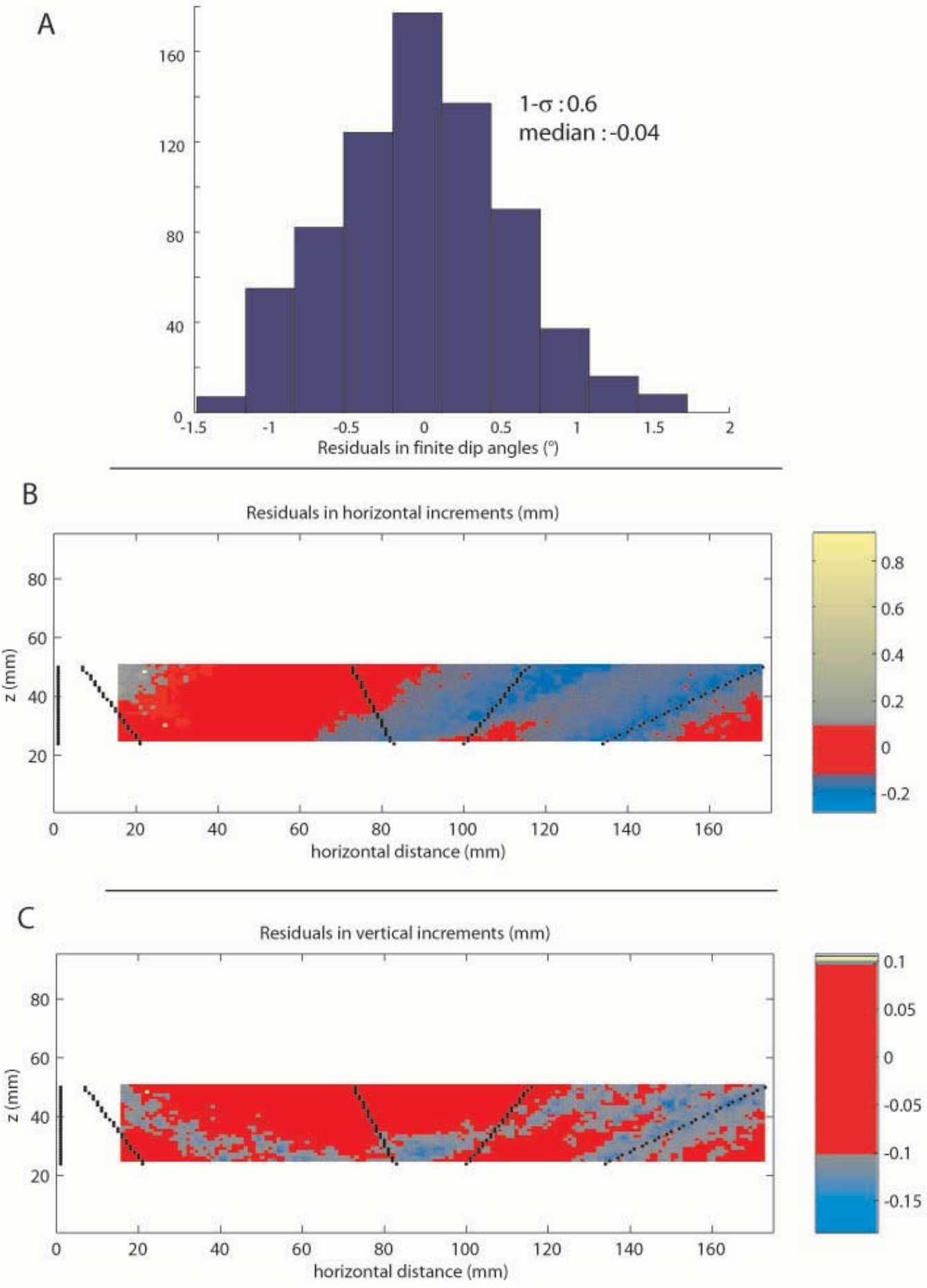
A
160
120
80
40
0
-1.5
-1
-0.5
0
0.5
1
1.5
2
1-σ : 0.6
median : -0.04
Residuals in finite dip angles (°)
B
Residuals in horizontal increments (mm)
z (mm)
horizontal distance (mm)
0.8
0.6
0.4
0.2
0
-0.2
C
Residuals in vertical increments (mm)
z (mm)
horizontal distance (mm)
0.1
0.05
0
-0.05
-0.1
-0.15

figure 21